N92-22748

PRIMARY ZINC-AIR BATTERIES FOR SPACE POWER

by

Bob Bragg and Debbie Bourland
NASA Lyndon B. Johnson Space Center
Houston, TX 77058

and

Glenn Merry and Ron Putt
MATSI, INC.
430 10TH ST NW STE S-007, Atlanta, GA 30318

INTRODUCTION

Zinc-air batteries are an excellent power source for aerospace use because they have the highest specific energy of all primary batteries (Table 1) and they are inherently safe.

Table 1: Primary Battery Specific Energies

System	Specific Energy (Wh/lb)
Alkaline-Manganese	60
Alkaline-Mercuric Oxide	55
Lithium-Sulfur Dioxide	125
Lithium-Manganese Dioxide	135
Zinc-Air	200

Despite decades of development there are currently only two types of zinc-air batteries on the market, button cells and low rate industrial batteries. Zinc-air button cells (Figure 1), used almost exclusively in hearing aids, are similar in design to zinc-mercuric oxide button cells, which they have displaced because of a twofold capacity advantage. The button cell configuration is an excellent means of packaging the zinc-air cell in small sizes (1 Ah or less), but scaleup to larger capacities has proven difficult because of performance and leakage problems.

Industrial zinc-air batteries are of a prismatic configuration which employ flat plate electrodes and a molded plastic case (Figure 2). Employed in low voltage railroad track signal circuits and in lighted aids to navigation, where a service life of 2-3 years is required, their maximum continuous drain rate is 1 A or less. Their full capacity is delivered only at drain rates below C/1200.

NASA-JSC has contracted with MATSI to expand zinc-air technology to two cell designs with high capacity and high rate capability, at specific energies which can only be met safely with zinc-air (Table 2).

Table 2: HR and LC Cell Specifications

Cell	Drain Rate	Capacity	Specific Energy
HR	1 A	12 Ah	160 Wh/lb
HR	3 A	9 Ah	-
LC	2 A	200 Ah	200 Wh/lb
LC	6 A	150 Ah	-

This has produced a novel prismatic design (Figure 3) which achieves the rate and specific energy targets and allows for stacking in multicell batteries. The thickness of the anode determines the capacity of the cell, and the area determines the maximum rate capability. An anode thickness of 0.5 cm, for example, produces an achievable specific capacity of 750 mAh/cm^2, while the maximum continuous current density is 50 mA/cm^2.

The next section discusses the a priori basis for our cell designs. This is followed by results of preliminary experimental work. Finally, we present data from parametric testing of HR and LC batteries.

DESIGN BASIS

The cell design (Figure 3) employs an anode paste of amalgamated zinc powder in a gelled potassium hydroxide electrolyte, a microporous polymeric separator, a porous, PTFE-bonded carbon oxygen electrode, and a plastic cell tray. Selection of anode thickness is dependent upon the specific capacity (mAh/cm^2) to be delivered and the utilization (%) achieved at a given current density. Figure 4 shows typical anode utilization data for a zinc-air button cell and for three sizes of alkaline cylindrical cells, all of which use similar anodes. The tailoff in the zinc-air cell curve is the result of air access restrictions to the cathode. The much lower utilizations for the alkaline cells are the result of the cylindrical geometry and the moisture uptake of the manganese dioxide cathode. We assumed AA utilizations for the initial designs, to be conservative, but those achieved in practice were more in agreement with the zinc-air curve, as extrapolated linearly.

The oxygen cathode is a high performance gas-diffusion electrode comprising two layers. The active layer on the electrolyte side employs high surface area carbon for the oxygen reduction reaction, and a metal oxide catalyst for peroxide decomposition. The barrier layer on the air side, having a higher PTFE content, prevents

electrolyte weepage. A microporous polymeric separator placed against the cathode surface prevents internal shorting.

Stacking cells in a battery requires that provision be made for air access to the cathodes. This is achieved by placing a porous spacer between cells. The thickness of this spacer is dependent on the lateral dimensions of the cell and the operating current density. If the spacer is too thin, interior portions of the cathode will become oxygen-starved, while too thick a spacer increases battery weight and volume unnecessarily.

An oxygen transport model was developed to assist in design of the intercell spacer. The model assumes only diffusion of oxygen through a stagnant nitrogen layer, since in space there is no natural convection, and forced convection of air to the cells is not assured. The model (Figure 5) assumes oxygen access from two sides only, and that the current distribution is uniform. It then calculates the spacer thickness (s) required for a given cell height (2L) and current density (i). Solution of the diffusion equation for this geometry yields the following relationship:

$$s = i \bullet L^2/1100.$$

That is, the minimum gap is proportional to the current density and the square of the path length for diffusion. Figures 6 and 7 show this relationship as applied to the LC and HR cells for three aspect ratios. Clearly, a low aspect ratio (height:width) is desirable for minimizing spacer thickness. Our design has therefore fixed on an aspect ratio of 1/2 for both cell designs.

Based on the above, the design points shown in Table 3 were set for the LC and HR cells.

Table 3: HR and LC Cell Design Specifications

Variable	HR Cell	LC Cell
Facial Dimensions	6 cm x 12 cm	13 cm x 25 cm
Thickness	0.7 cm	0.8 cm
Weight	93 g	540 g
Spacer Thickness	0.6 cm	0.8 cm
Capacity	30 Ah @ 1 A	204 Ah @ 2 A
Specific Energy	170 Wh/lb @ 1 A	210 Wh/lb @ 2 A

PRELIMINARY DEVELOPMENT

A series of experiments was conducted on subscale prototype cells to test the elements of the design basis and to optimize electrode

formulations. The first set focussed on anode optimization. Test cells were discharged at four different zinc contents (weight percentages), and their specific capacities were calculated. The data in Figure 8 indicate that, while there are no substantial differences statistically, a zinc content of 70% consistently performed well, and so it became the standard.

Another set of experiments elucidated the sensitivity of anode utilization to KOH concentration. Two concentrations, 30% and 35%, were tested at two ambient relative humidities, 35% and those in equilibrium with the two electrolyte concentrations (58% RH and 47% RH, respectively). The data shown in Figure 9 show that utilization is consistently higher for the 35% KOH concentration, and for that concentration the utilization is less sensitive to low ambient relative humidity. The 35% concentration therefore became the standard.

The cathode optimization studies showed the need for a peroxide decomposition catalyst, not only for improved cell voltage, but also for improved anode utilization. Figure 10 shows that anode utilization is substantially higher when the catalyst is used. The weight gain data, expressed as the quotient of cell weight after and before discharge (over and above the weight gain calculated for oxygen uptake based on delivered capacity, *i.e.* 0.3 g/Ah), indicate that the no-catalyst cell anodes were non-faradaically converted to oxide because of peroxide migration and reaction there. In other words, the peroxide acts as a soluble form of oxygen which, if not decomposed in the pores of the cathode, acts to corrode the zinc in a direct chemical reaction.

Finally, the discharge data for more than 40 cells were employed to create an empirical model of cell performance. Figure 11 shows the derived relationship between utilization and current density, and Figure 12 relates average cell voltage to current density. These are expressed mathematically as follows:

$$U\ (\%) = 97 + 32\ln(1 - i/70), \text{ and}$$

$$Vav\ (V) = 1.29 - 0.0058i.$$

Based upon this model, the sensitivity of specific energy to anode thickness for the HR cell was calculated (Figure 13), which showed the need for a 0.4 cm thick anode to meet the 160 Wh/kg requirement at a 1 A drain rate.

BATTERY TESTING

The HR and LC cell designs were finalized based on the preliminary experimental work, and cells were built and tested both as individual cells and as five cell batteries. Figure 14 shows the individual HR and LC cells, and Figure 15 shows a five cell LC battery. A typical load curve at 100% state-of-charge for an HR cell (LC is similar) is shown in Figure 16. The trace curves

upward toward an open circuit voltage of 1.4 V below 5 mA/cm^2, but is essentially linear at higher current densities.

Typical cell discharge curves at 25° C are shown in Figures 17 and 18 for the three currents tested. Cell voltages are relatively flat throughout most of the discharge, their negative slope and curvature proportional to the drain rate. The voltage knee is fairly sharp, with little capacity beyond the 0.9 V cutoff value. Capacity dependence on current is shown in Figures 19 and 20.

Individual cell data points for each of the three drain rates and temperatures tested are shown in Figures 21 and 22 (HR), and Figures 23 and 24 (LC), along with the empirical model data for 25° C. The HR data show good performance relative to the model predictions under all conditions except the 2 and 3 A runs at 50° C. For these runs forced air circulation was required in the test oven to ensure adequate oxygen supply to the batteries, and this accelerated dryout of the cells, which lowered utilization.

LC battery utilizations were consistently below model predictions at all temperatures tested because of dryout, in what we term a chimney effect. The cells ran at least 20° C warmer than ambient, and this, in combination with oxygen depletion, produced an updraft of air in the intercell spacers which enhanced dryout. The most dramatic evidence of this is shown in Figures 25 and 26. Figure 25 shows utilization by cell for the 6 A, 25° C run. Utilization is at a minimum for Cell 3, the center cell, and is at a maximum for cells 1 and 5, the end cells. Figure 26 shows the water loss data for this test, cell by cell, with a maximum in the center and lower values at the ends. While there is not a reproducibly uniform dependence of utilization on water loss (accelerated localized dryout can be as much a detriment as uniform dryout), the generally high electrolyte weight (moisture) losses observed (as high as 43%) account for the suppressed utilizations. Water loss data are compared in terms of flux (g/h/cm^2) versus current density in figure 27 for HR and LC cells. Water flux for the LC batteries is approximately a factor of ten higher than that for the HR batteries when compared at equivalent current densities.

The chimney effect can be mitigated, for testing at 1 G, by reducing air access to and thickness of the intercell spacers. In space, at 0 G, there would be no chimney effect, and utilizations would likely be much higher. Furthermore, if the batteries were fed pure oxygen at a stoichiometric rate, dryout could be reduced to near zero, as could the spacer thickness.

Water loss data are compared in terms of flux (g/h/cm^2) versus current density in Figure 27 for HR and LC batteries. Water flux for the LC batteries is about a factor of 10 higher than that for HR batteries, when compared at equivalent current densities. This is probably the result of cell size and intercell spacer thickness differences between the two designs.

CONCLUSION

The prismatic HR and LC cells and batteries built and tested performed well with respect to the program goals (Table 4).

Table 4: HR and LC Cell Performance (@ 25° C)

Cell Type	Drain Rate	Capacity		Specific Energy (Wh/lb)	
		Goal	Achieved	Goal	Achieved
HR	1 A	12 Ah	29 Ah	160	165
HR	3 A	9 Ah	24 Ah	-	131
LC	2 A	200 Ah	203 Ah	200	211
LC	6 A	150 Ah	188 Ah	-	182

The HR batteries suffered reduced utilizations owing to dryout at the 2 and 3 A rates for the 50° C tests owing to the requirement for forced convection. The LC batteries suffered reduced utilizations under all conditions owing to the chimney effect at 1 G, although this effect would not occur at 0 G. An empirical model was developed which accurately predicted utilizations and average voltages for single cells, although thermal effects encountered during battery testing caused significant deviations, both positive and negative, from the model. Based on the encouraging results of the test program, we believe that the zinc-air primary battery of a flat, stackable configuration can serve as a high performance and safe power source for a range of space applications.

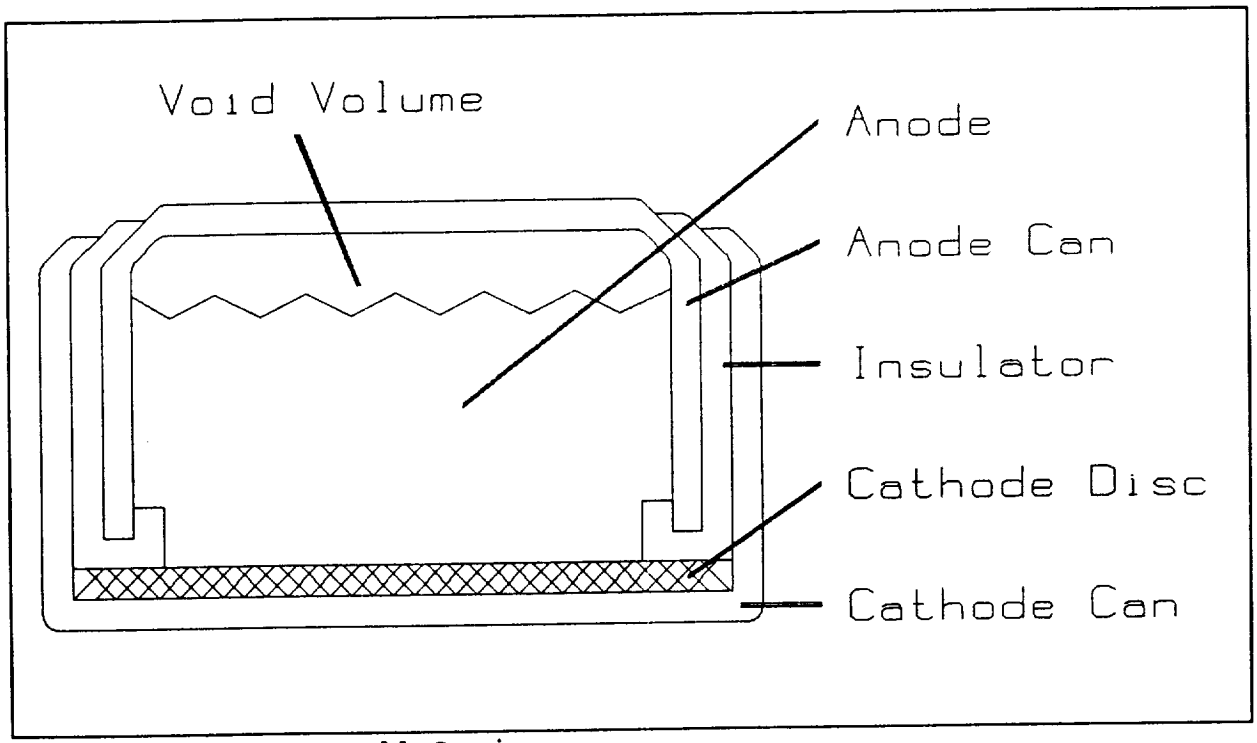

Figure 1: Button Cell Design

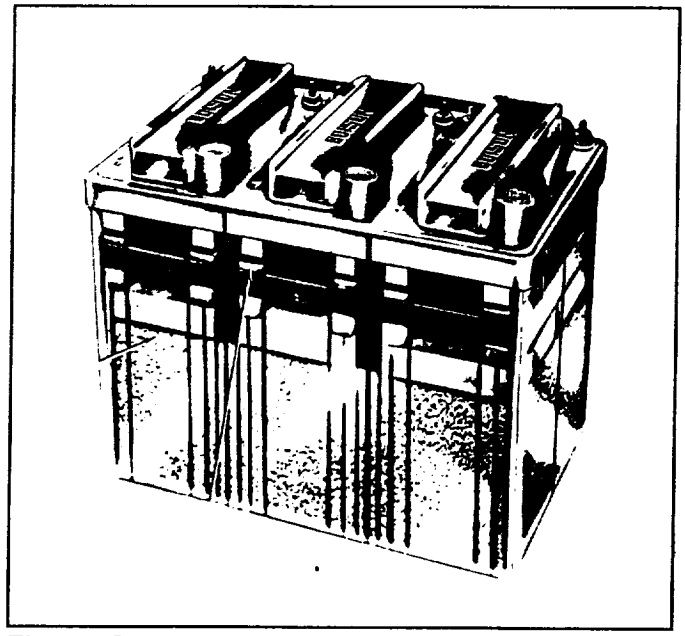

Figure 2: Industrial Zinc-Air Battery

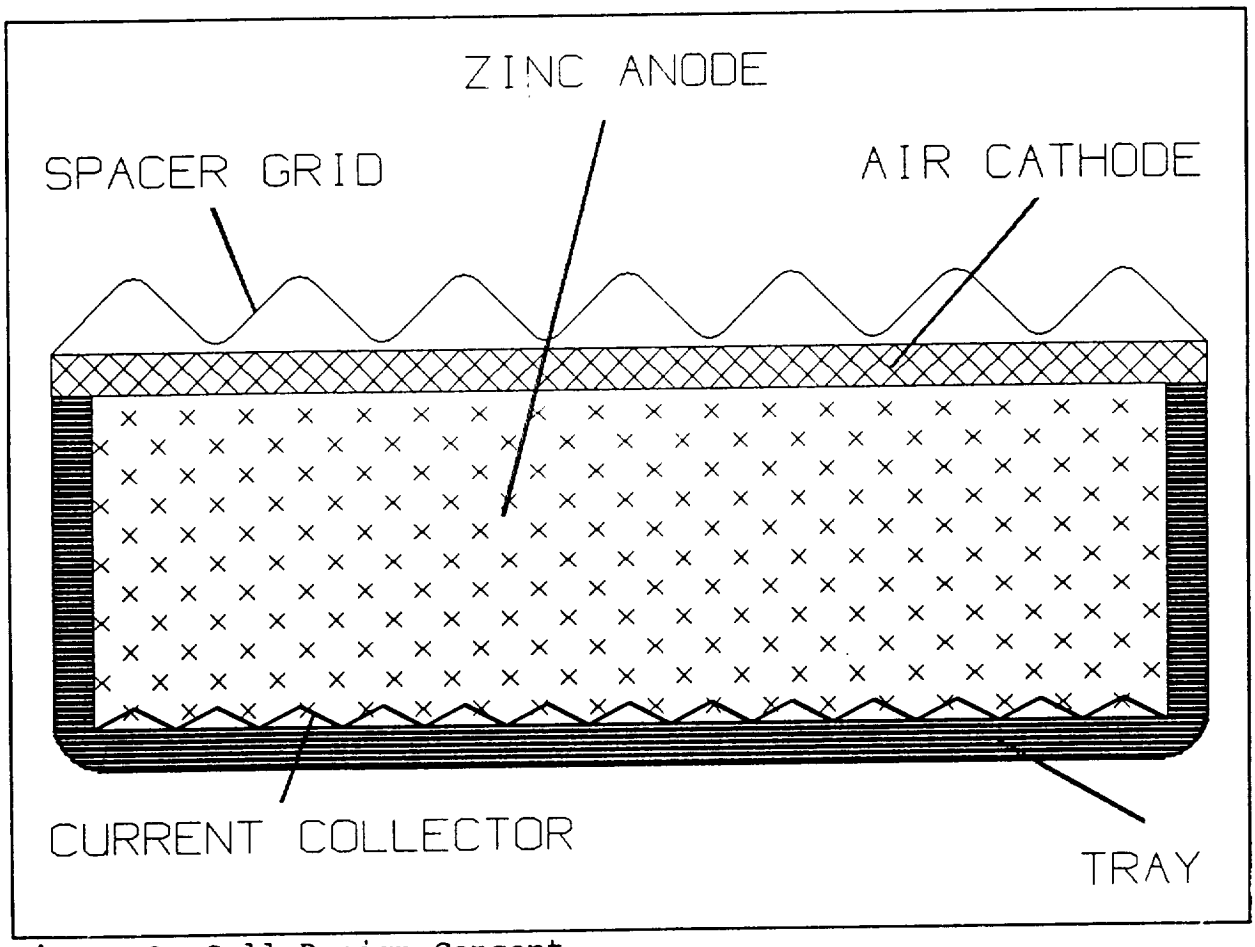

Figure 3: Cell Design Concept

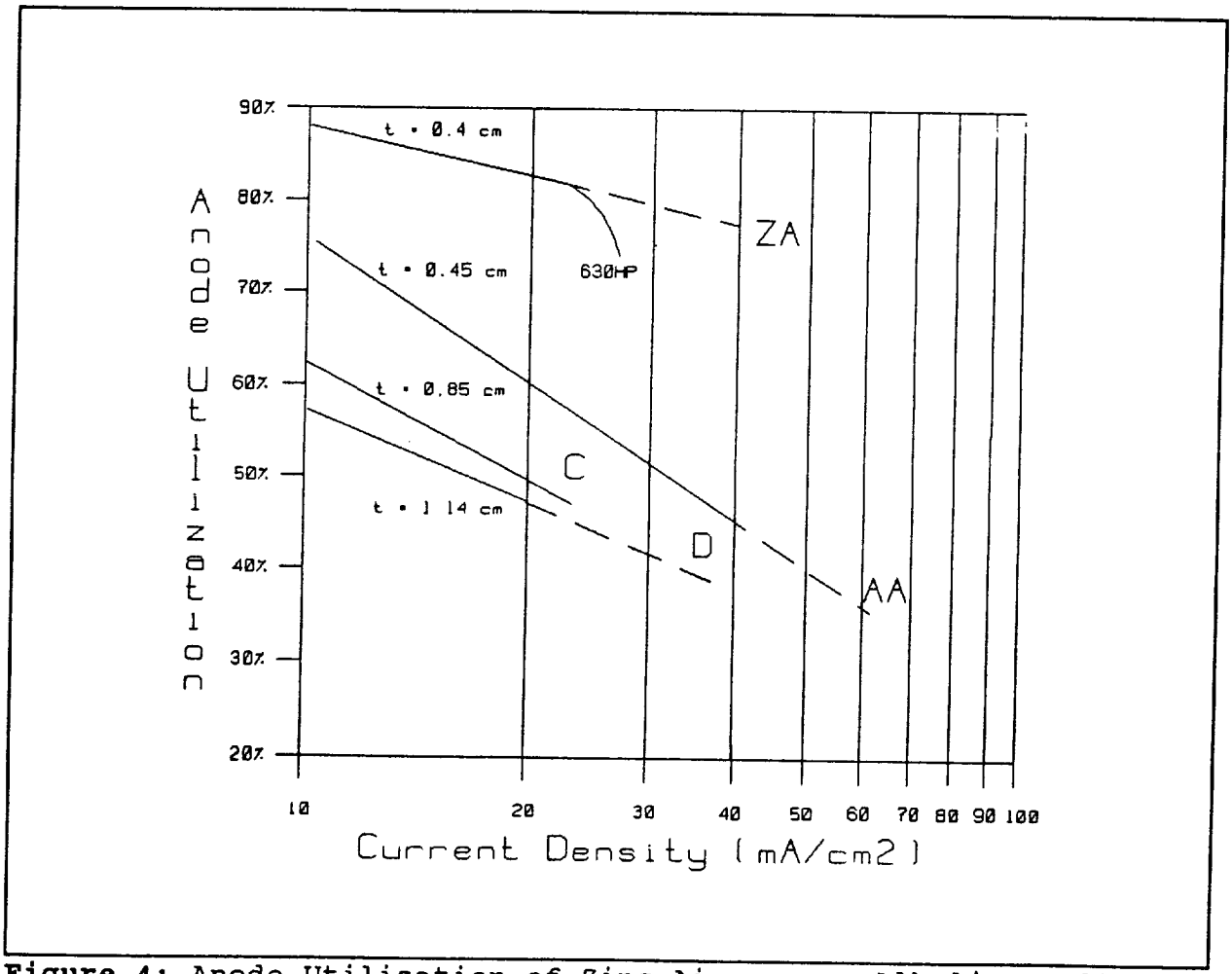

Figure 4: Anode Utilization of Zinc-Air versus Alkaline Cells

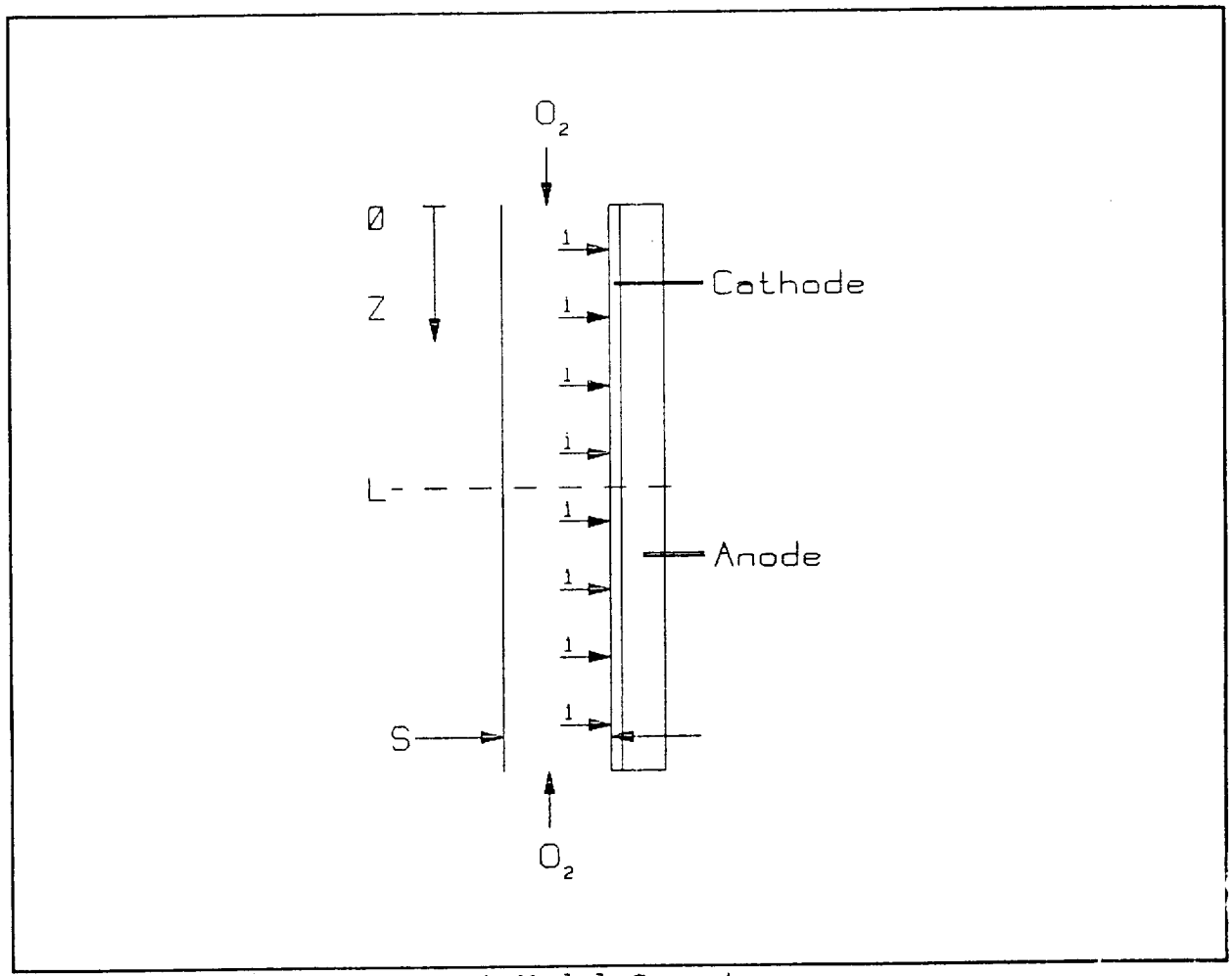

Figure 5: Oxygen Transport Model Geometry

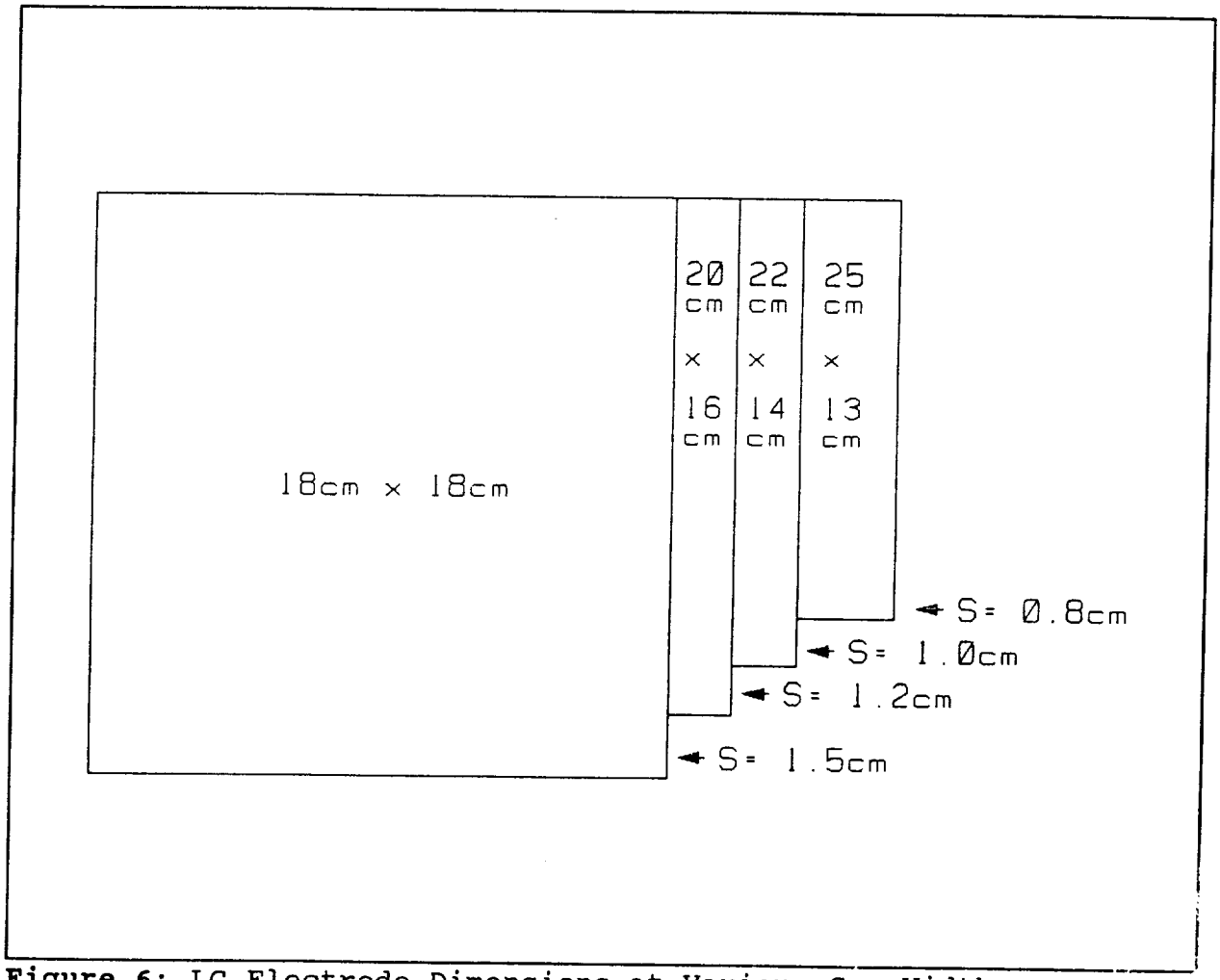

Figure 6: LC Electrode Dimensions at Various Gap Widths

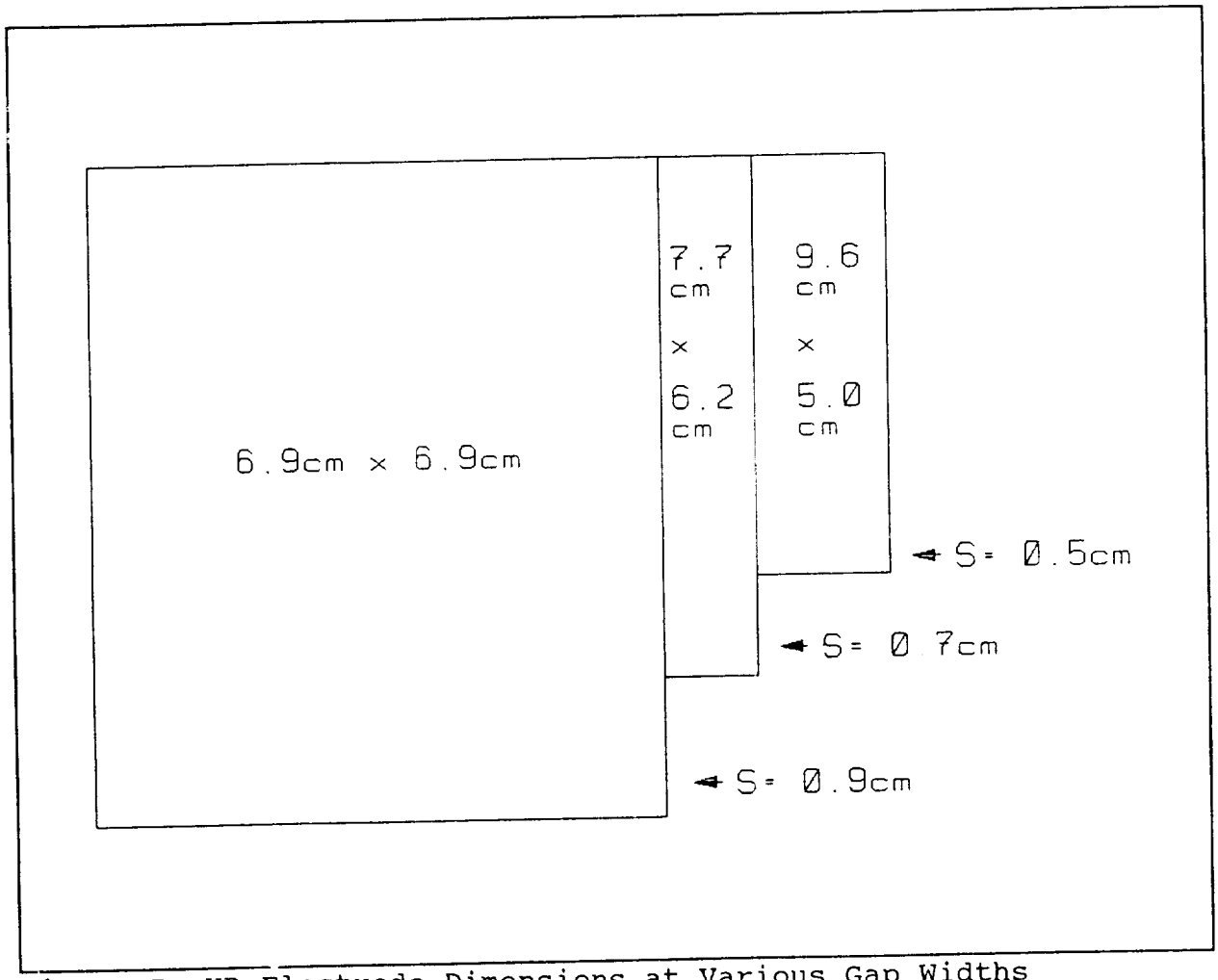

Figure 7: HR Electrode Dimensions at Various Gap Widths

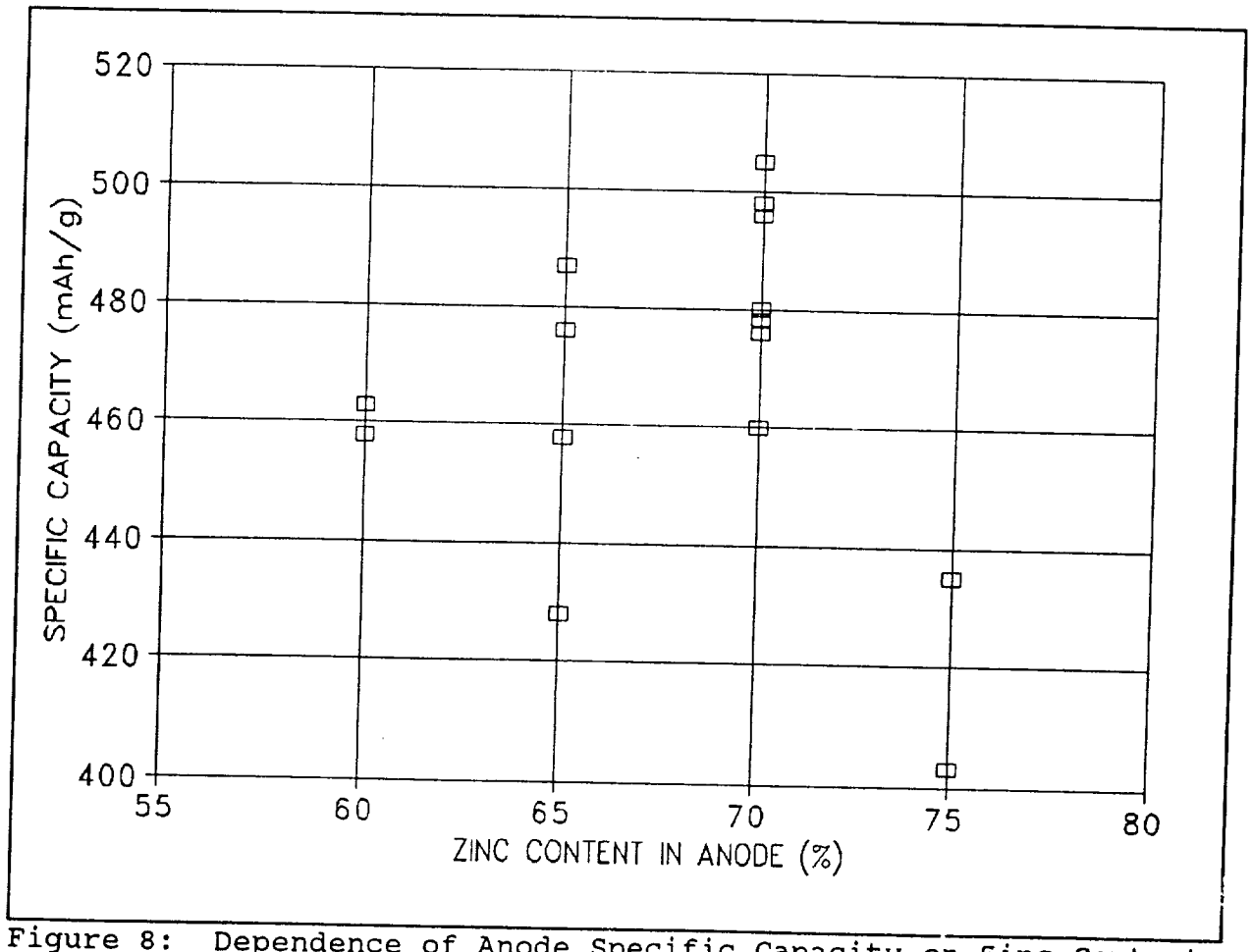

Figure 8: Dependence of Anode Specific Capacity on Zinc Content

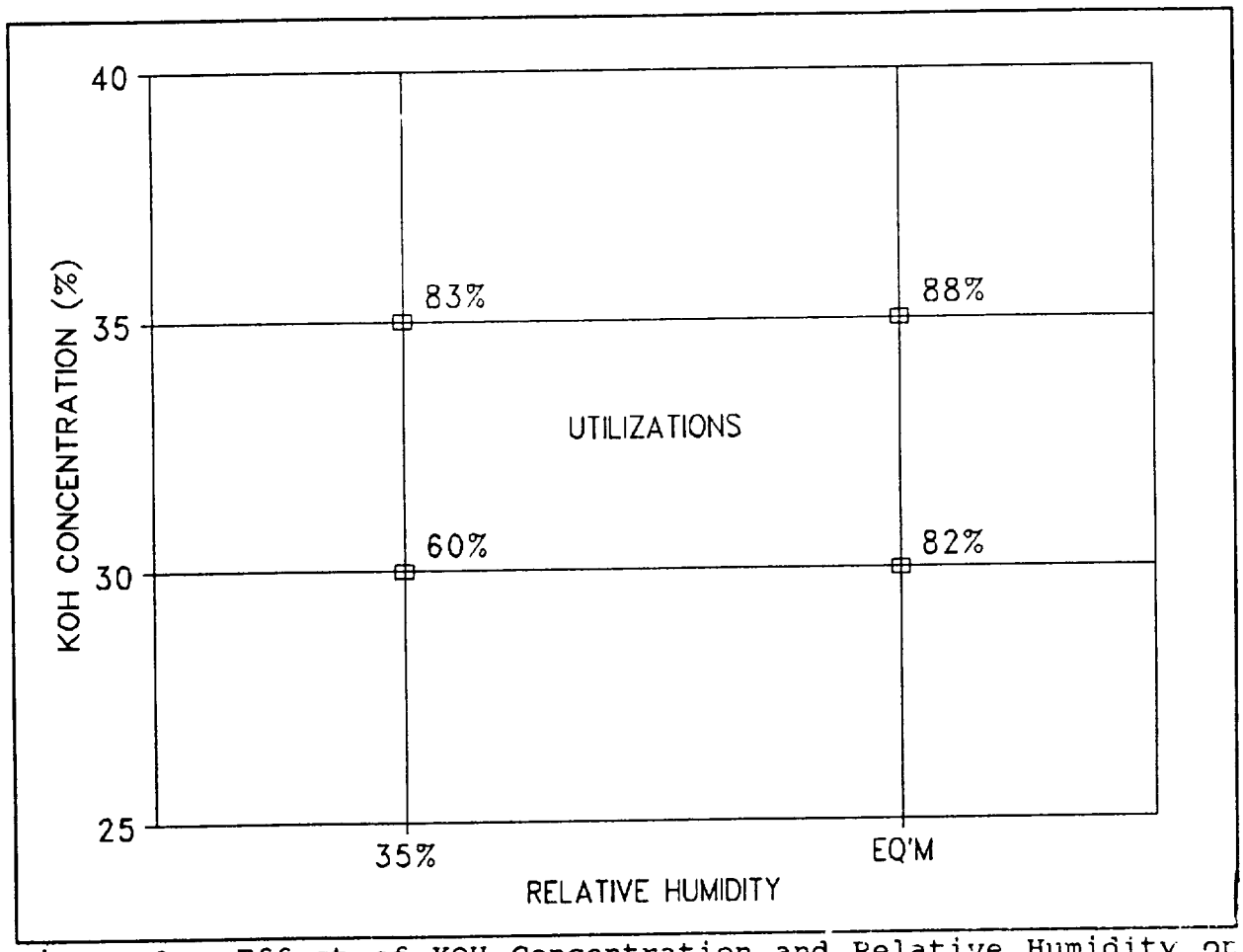

Figure 9: Effect of KOH Concentration and Relative Humidity on Anode Utilization

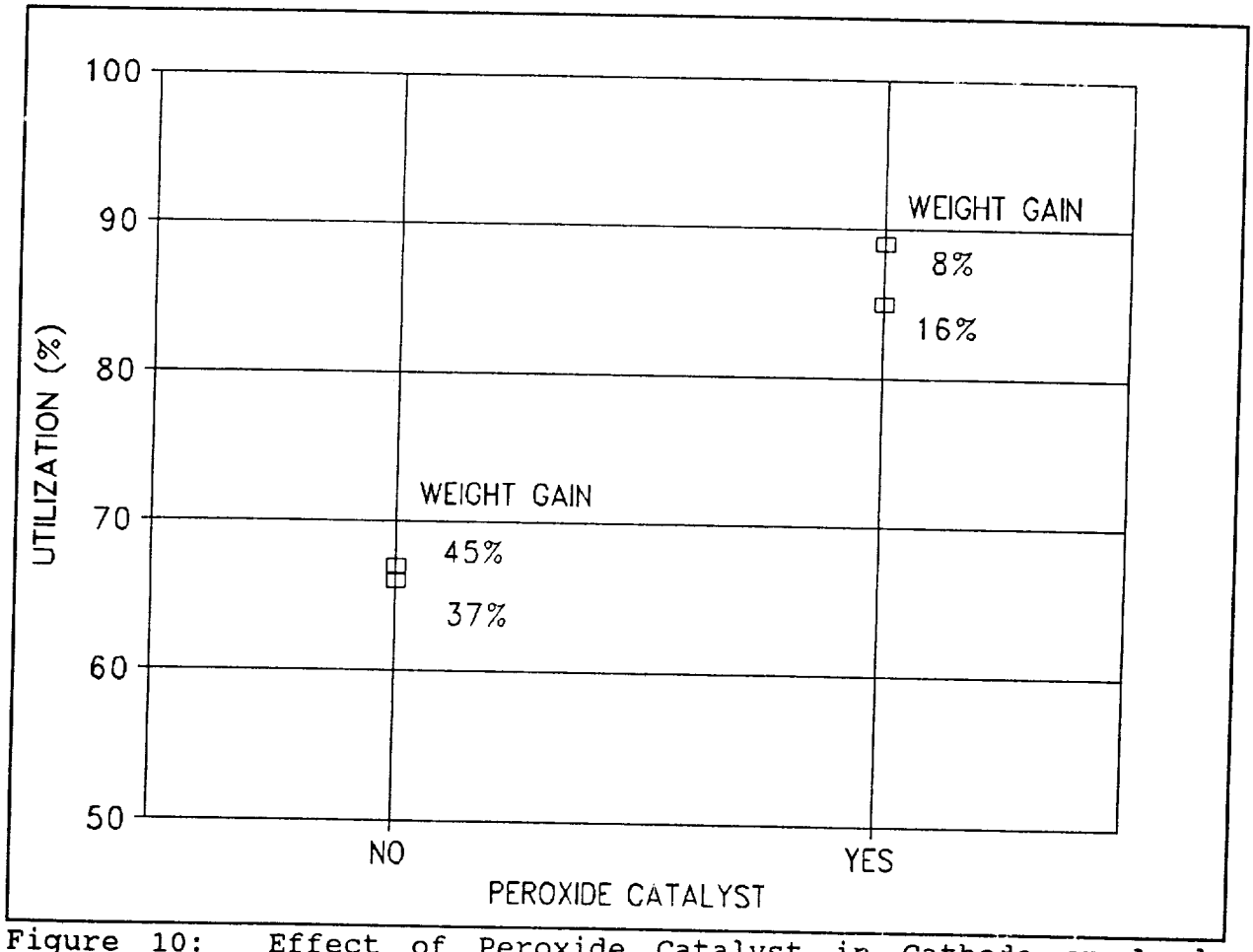

Figure 10: Effect of Peroxide Catalyst in Cathode on Anode Utilization

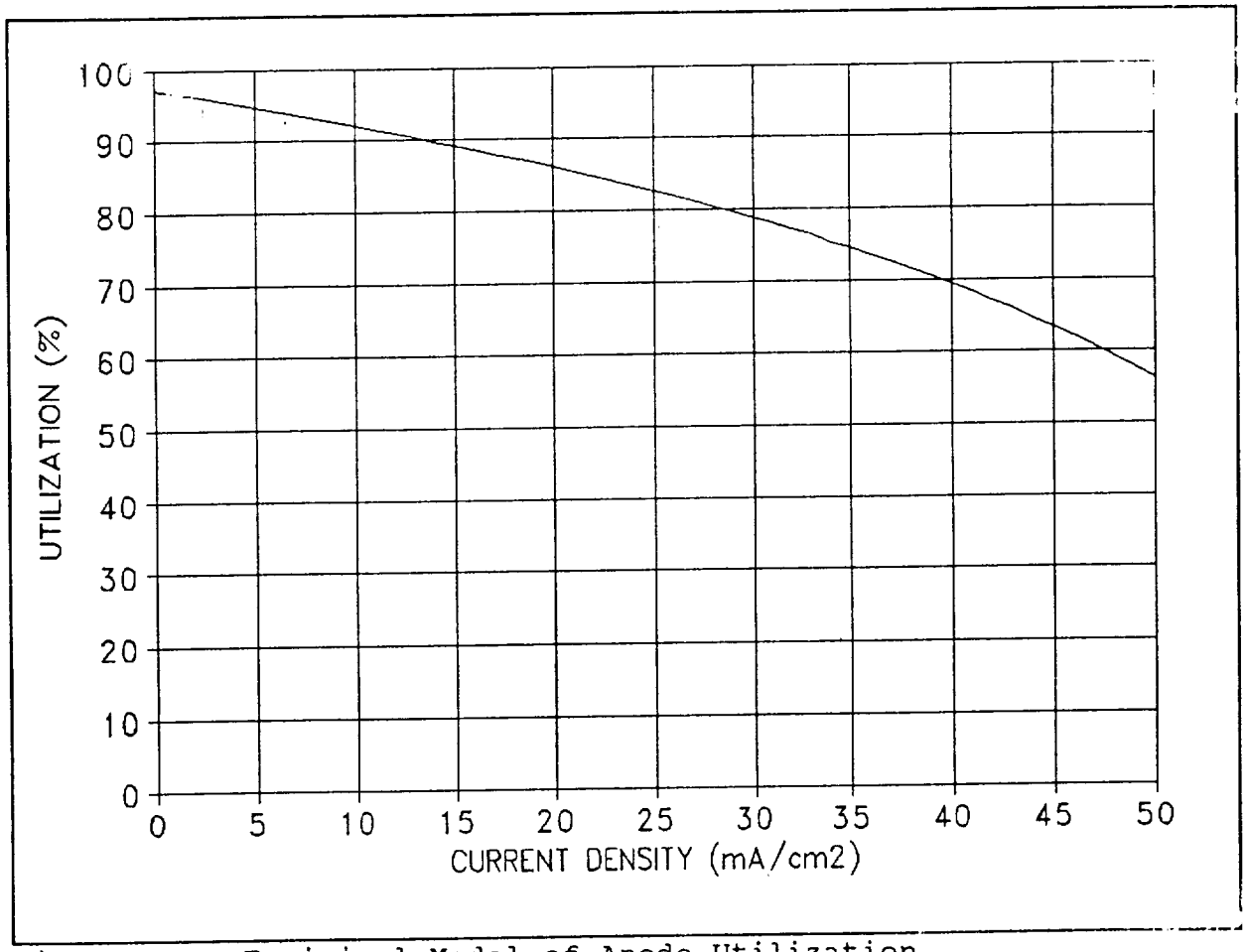

Figure 11: Empirical Model of Anode Utilization

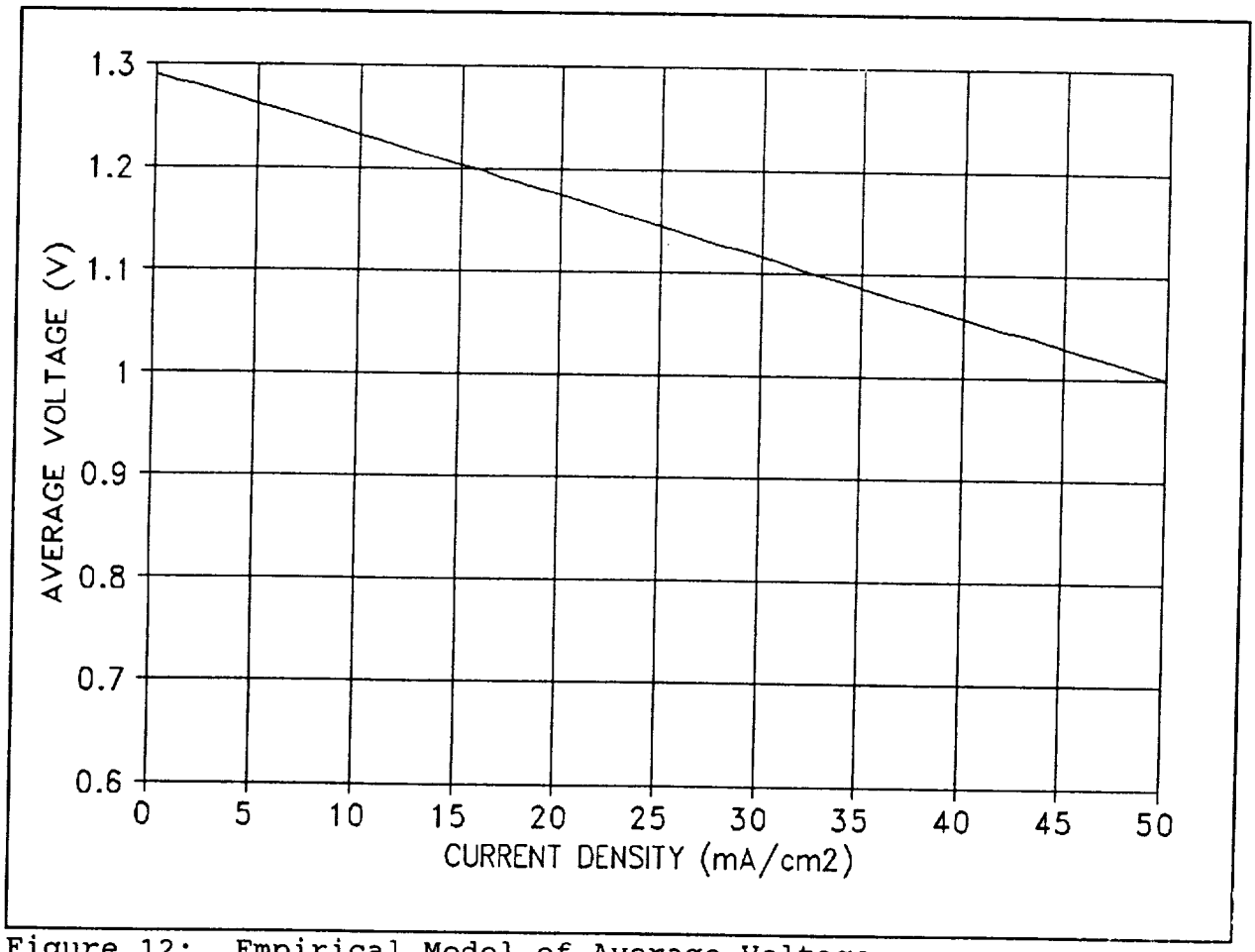

Figure 12: Empirical Model of Average Voltage

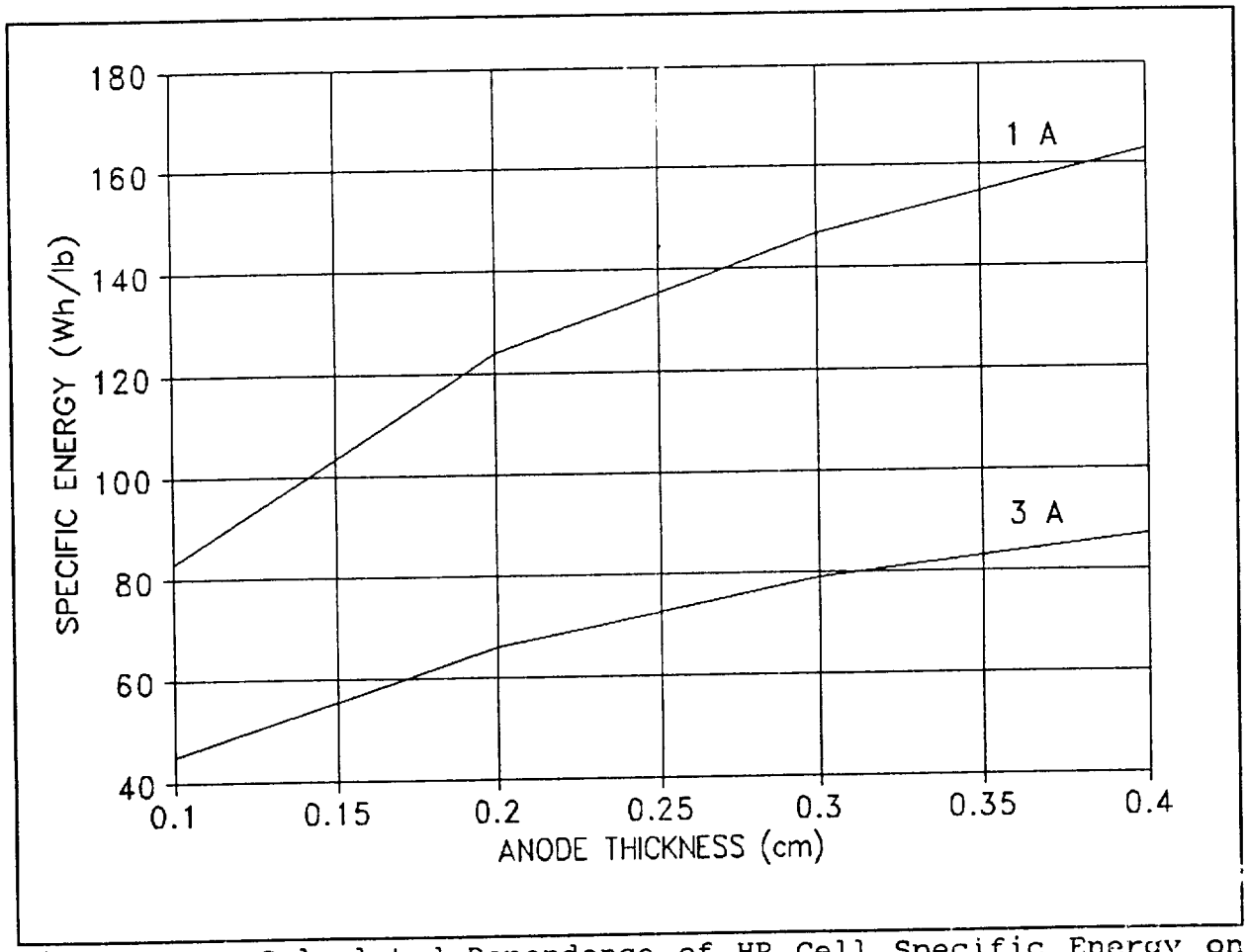

Figure 13: Calculated Dependence of HR Cell Specific Energy on Anode Thickness

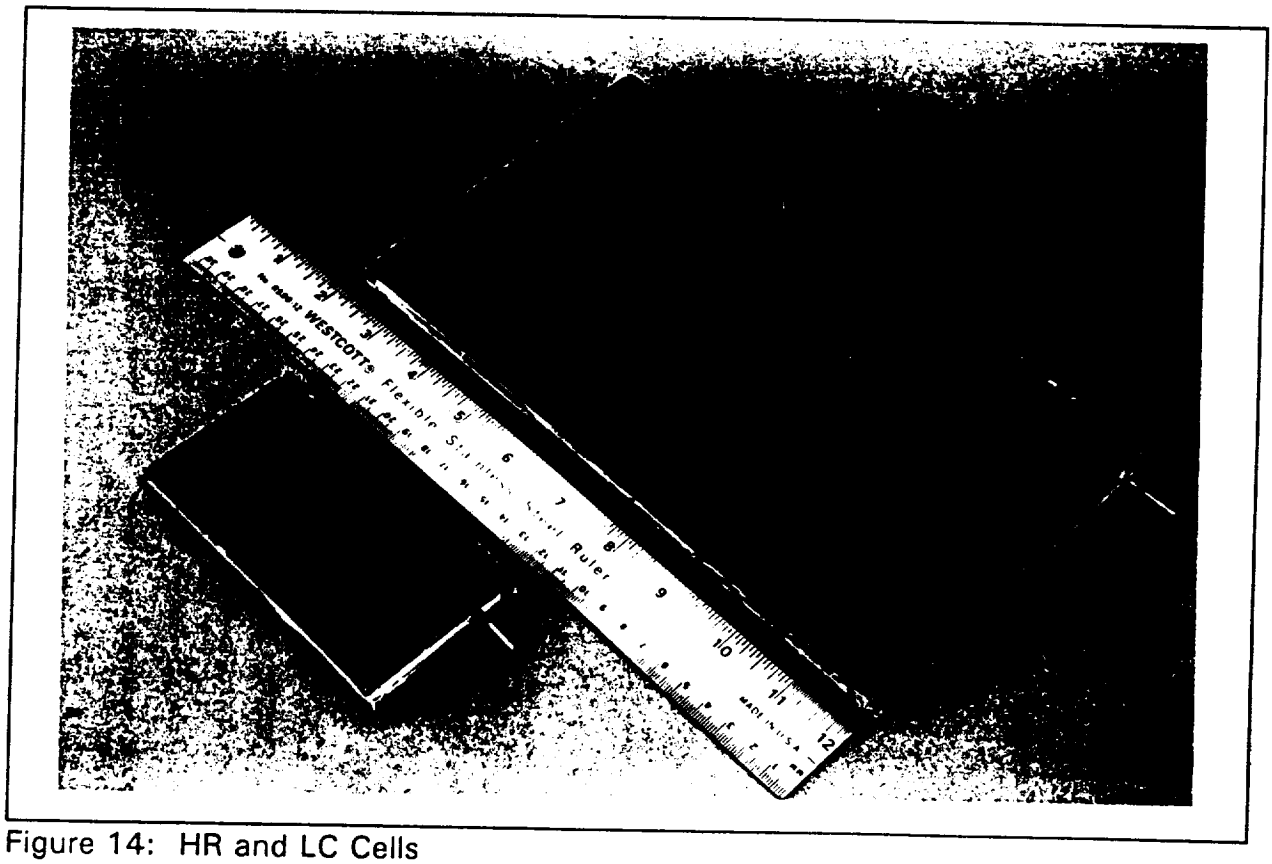

Figure 14: HR and LC Cells

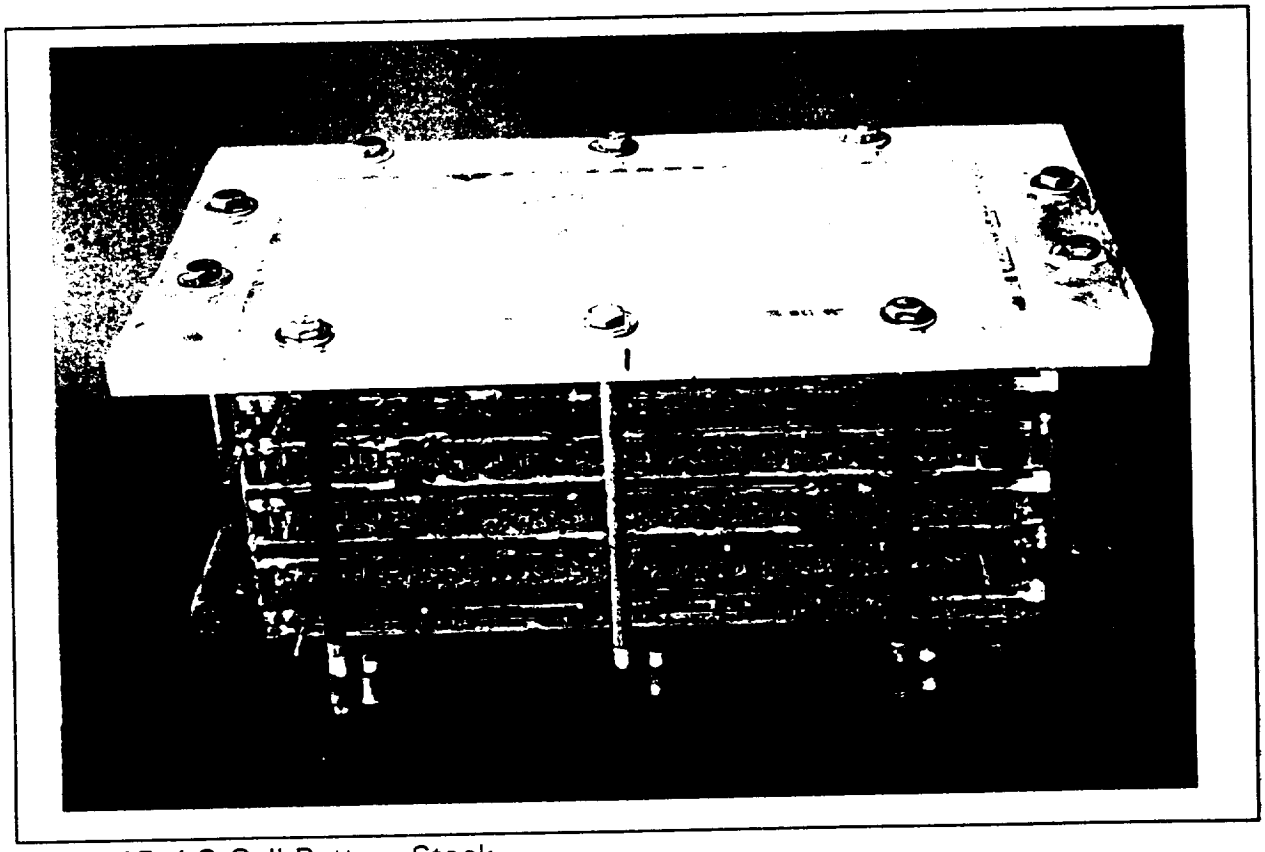

Figure 15: LC Cell Battery Stack

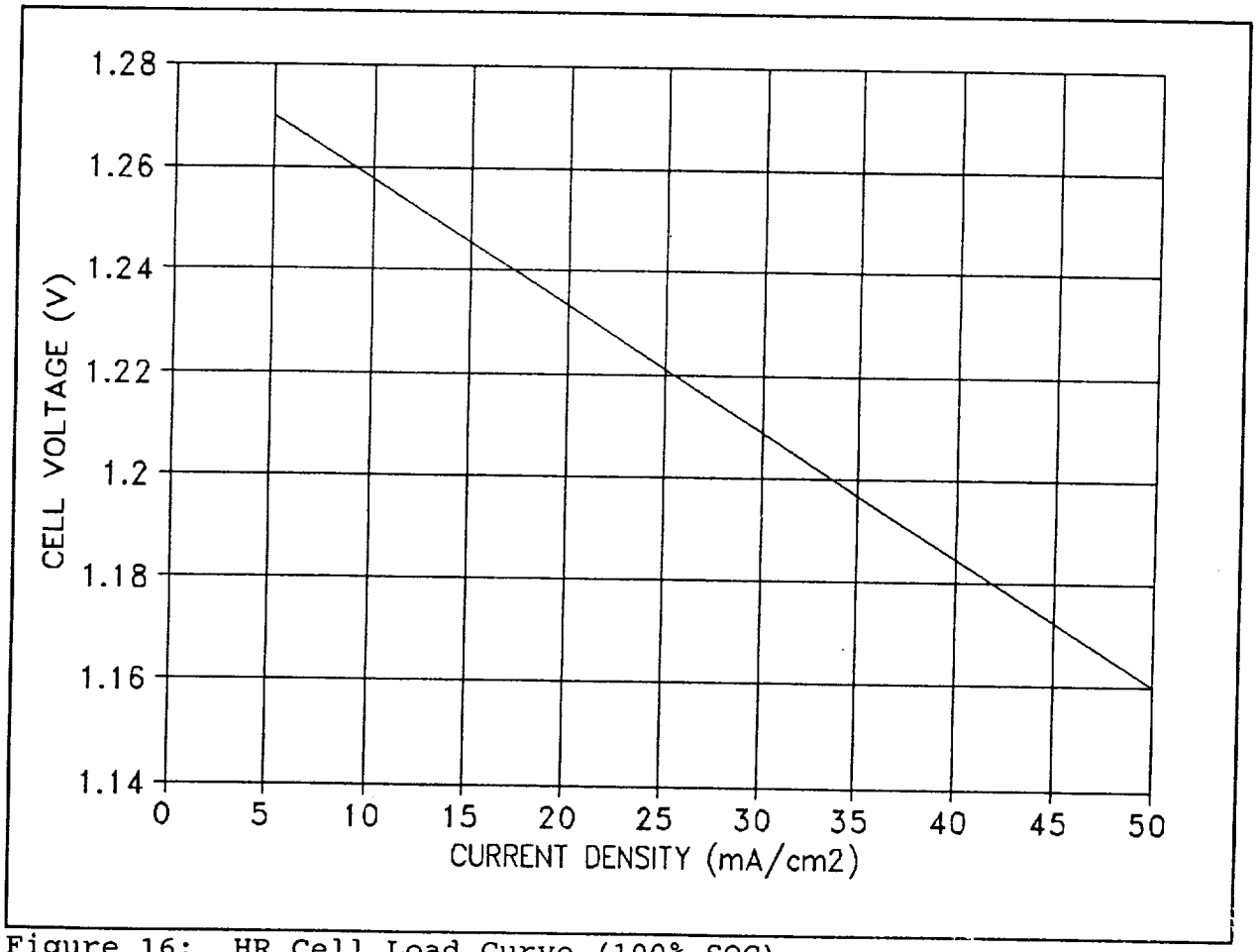

Figure 16: HR Cell Load Curve (100% SOC)

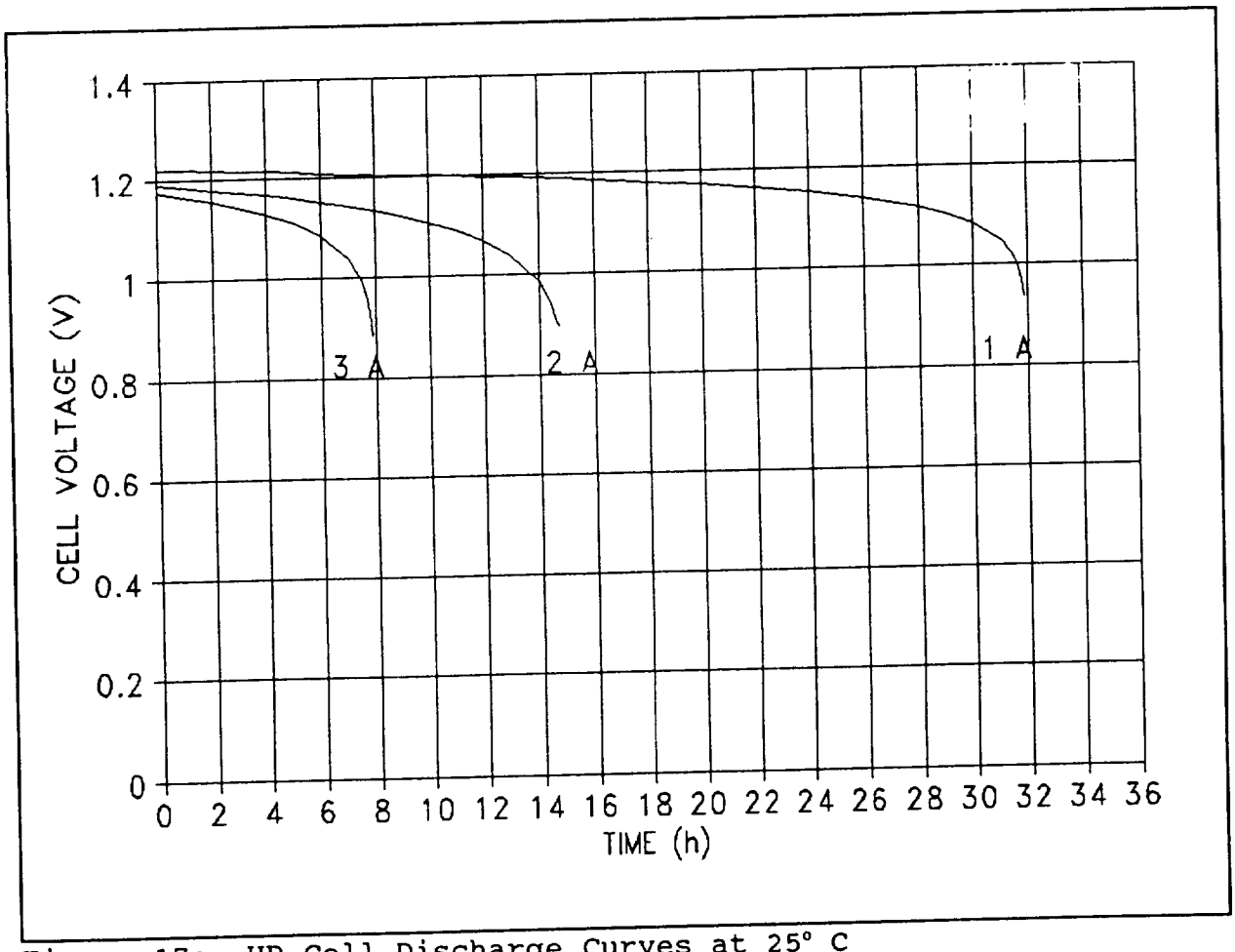

Figure 17: HR Cell Discharge Curves at 25° C

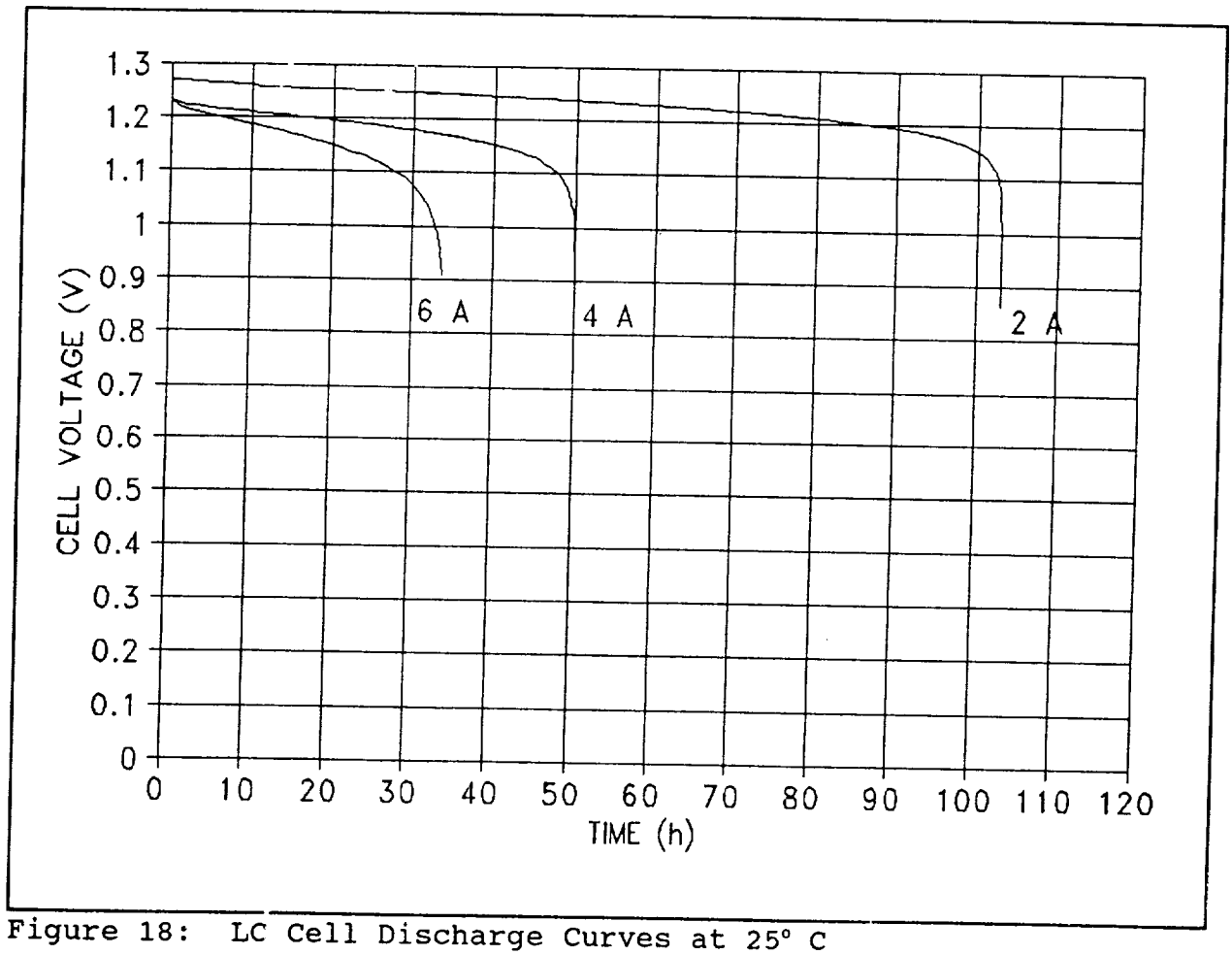

Figure 18: LC Cell Discharge Curves at 25° C

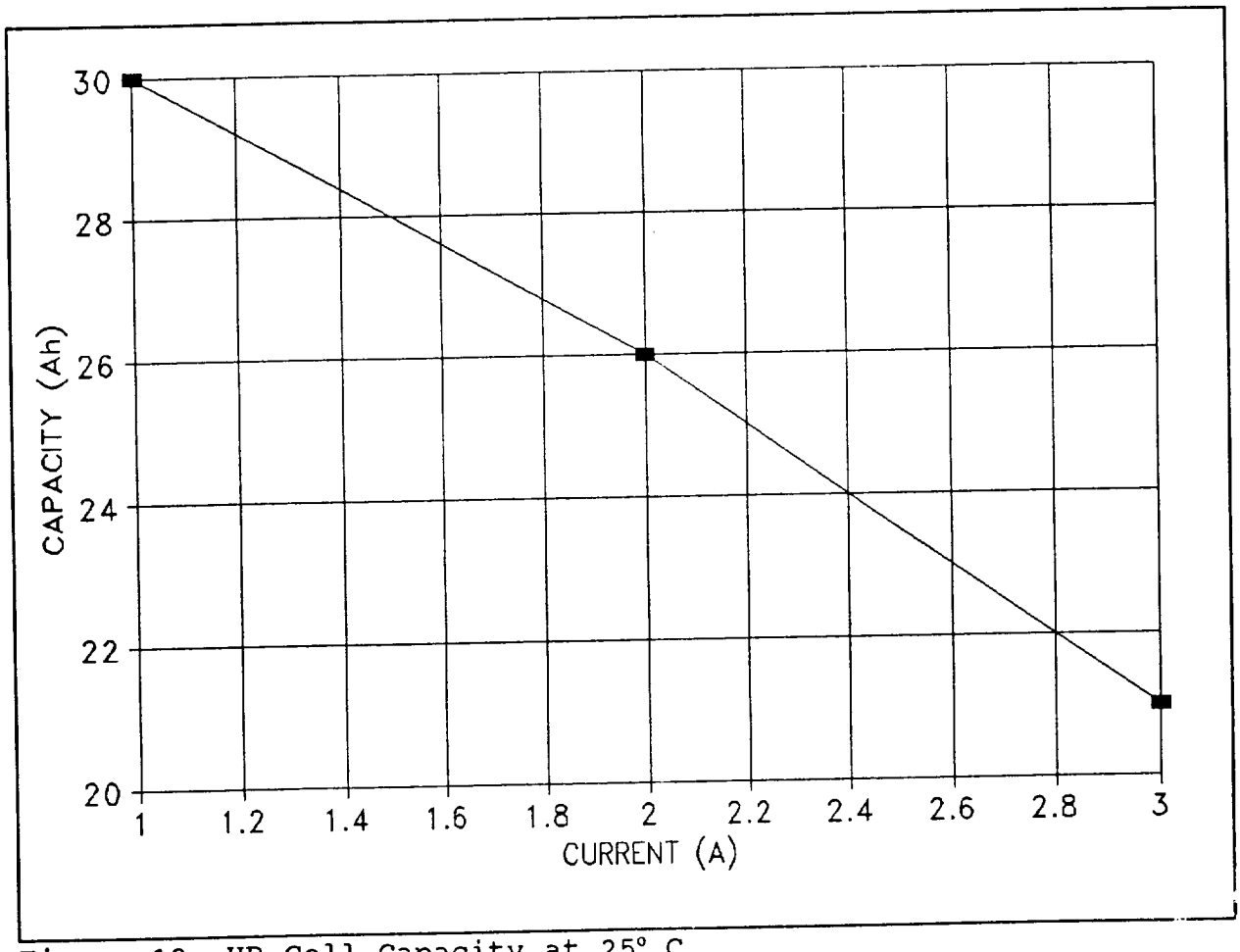

Figure 19: HR Cell Capacity at 25° C

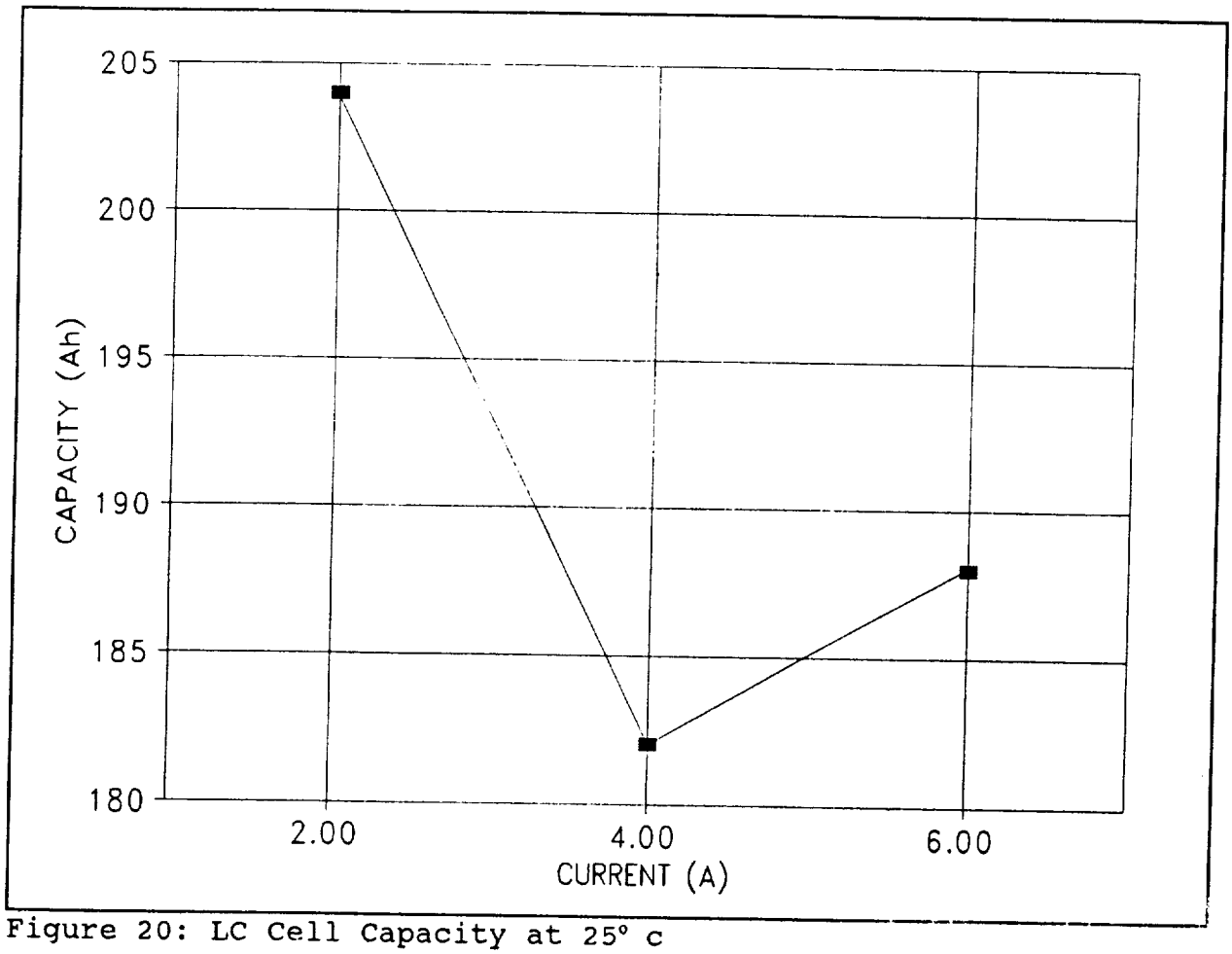

Figure 20: LC Cell Capacity at 25° c

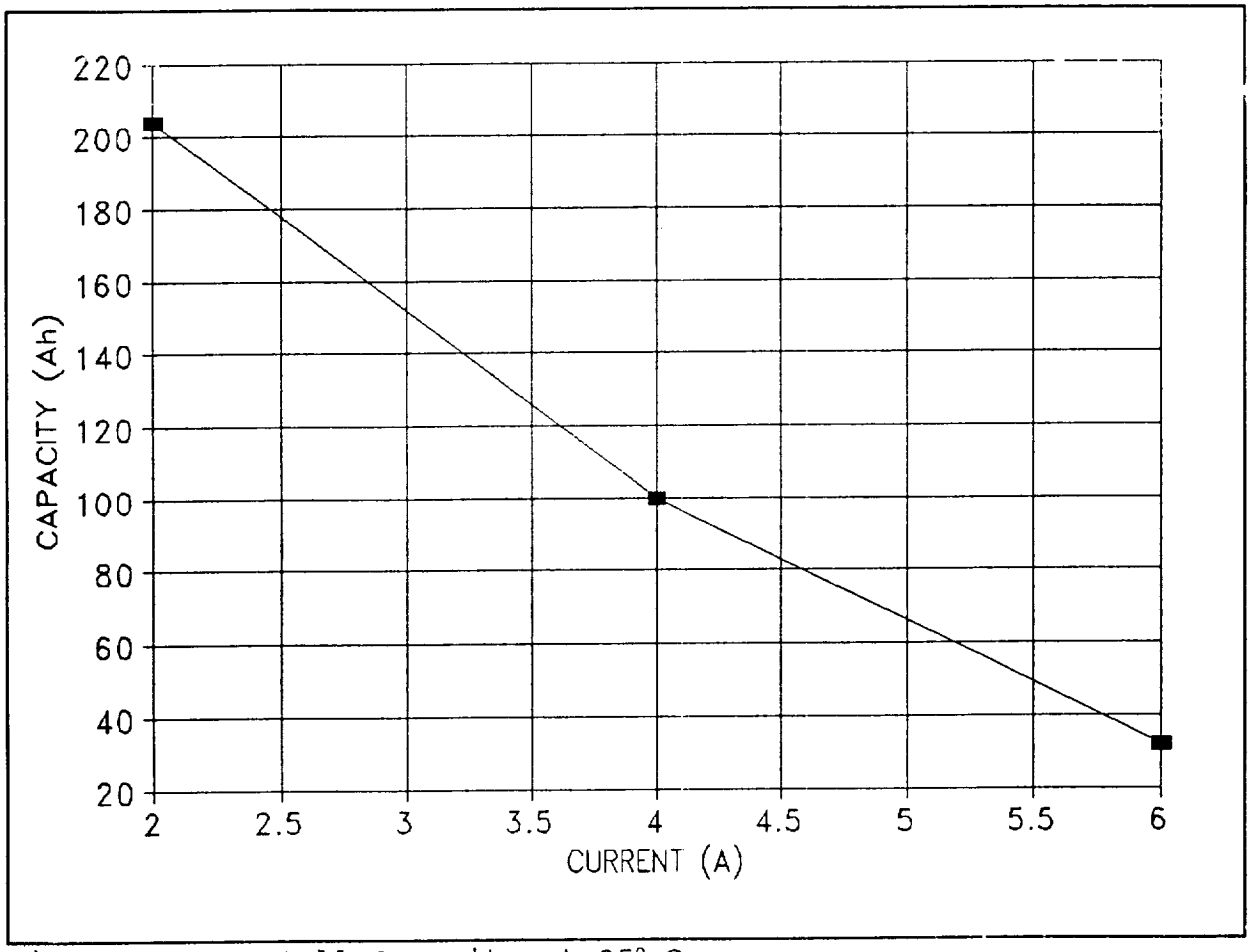

Figure 20: LC Cell Capacity at 25° C

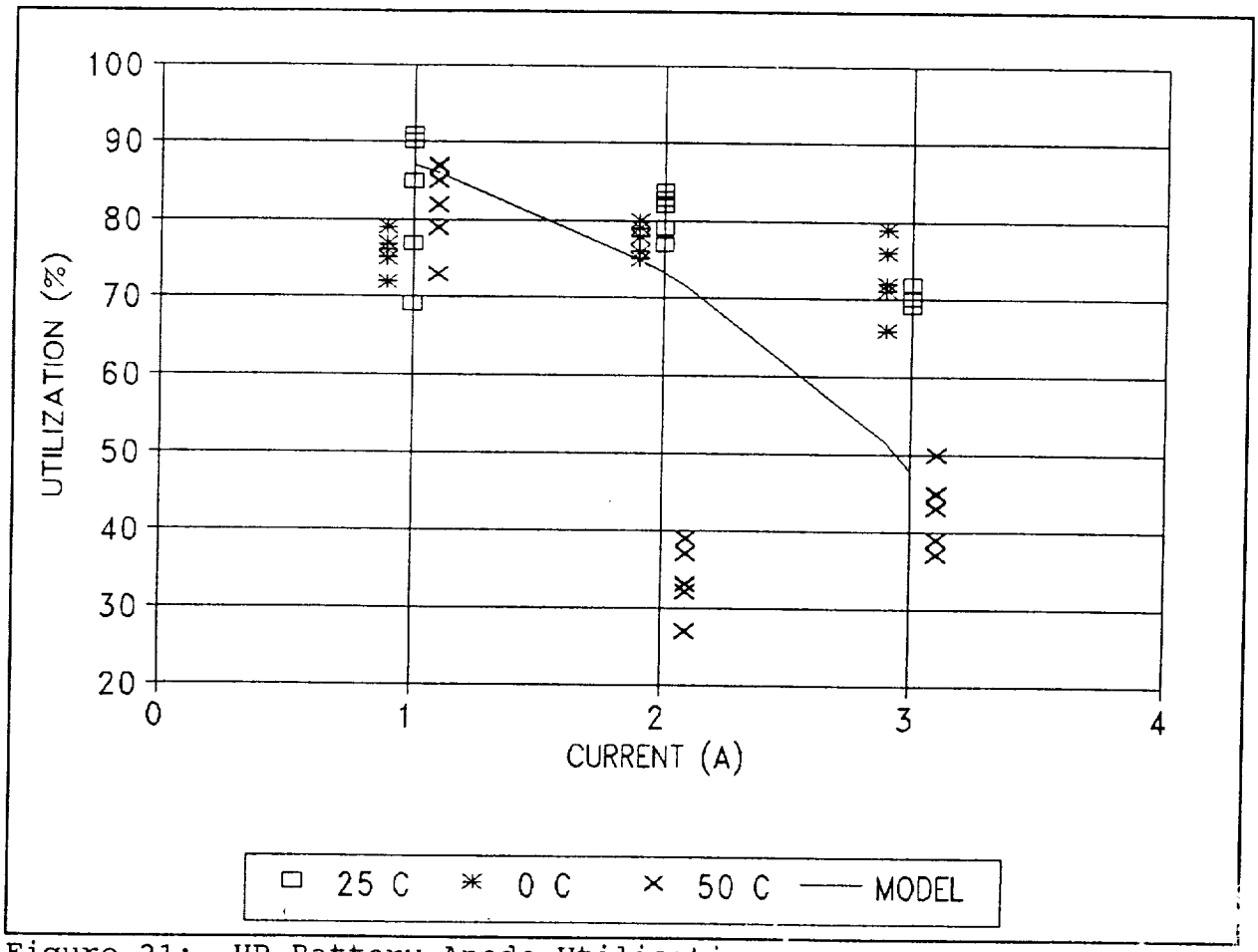

Figure 21: HR Battery Anode Utilization

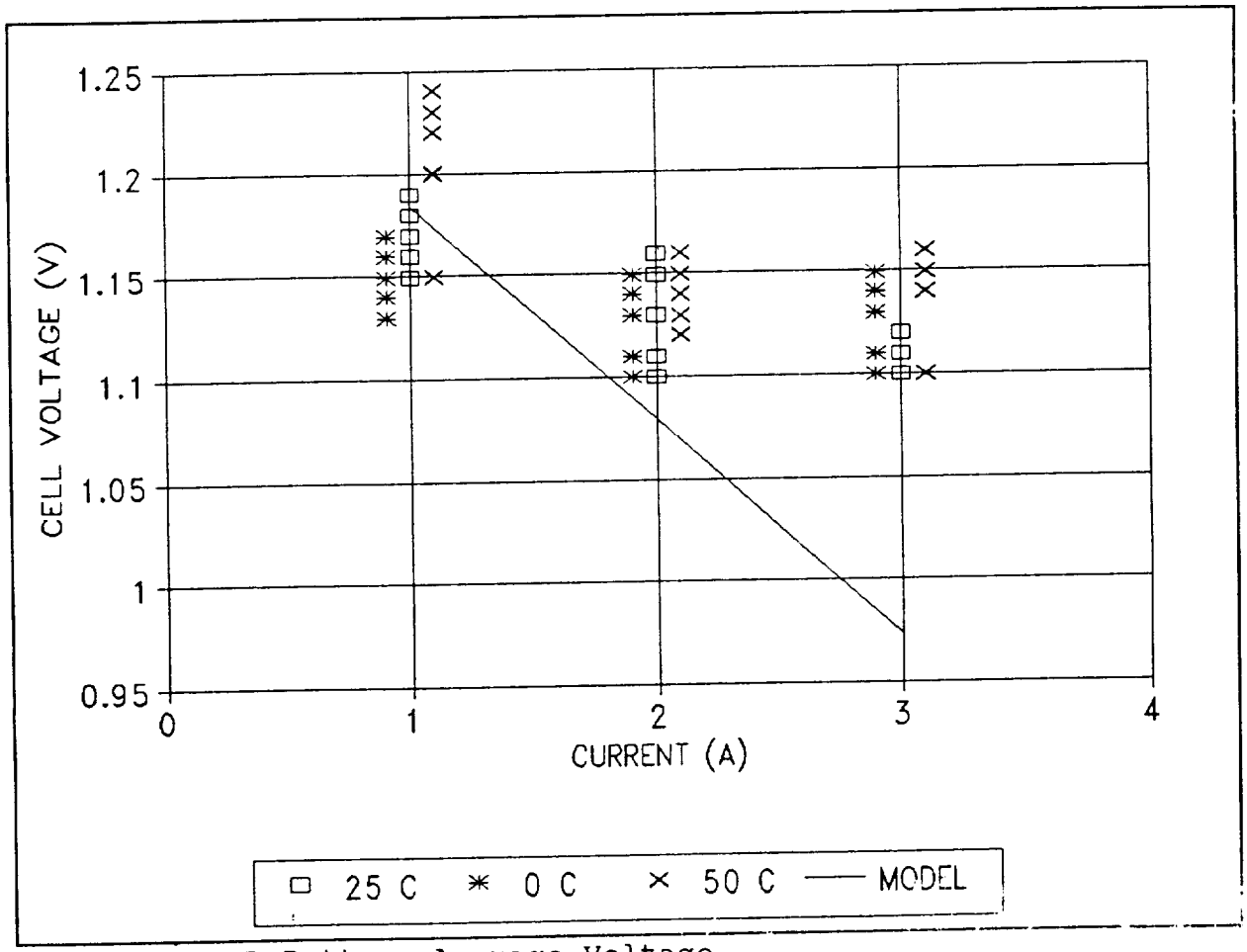

Figure 22: HR Battery Average Voltage

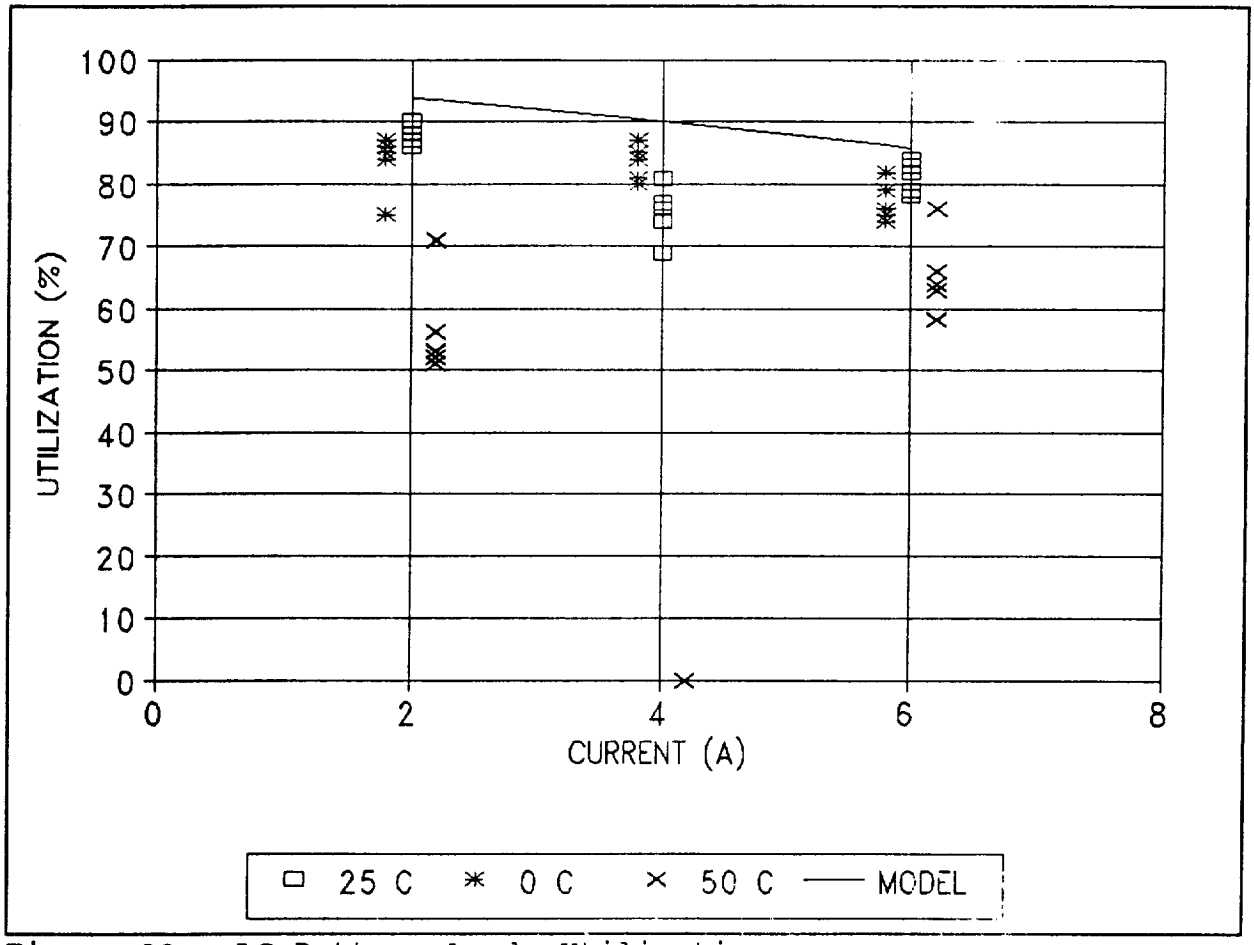

Figure 23: LC Battery Anode Utilization

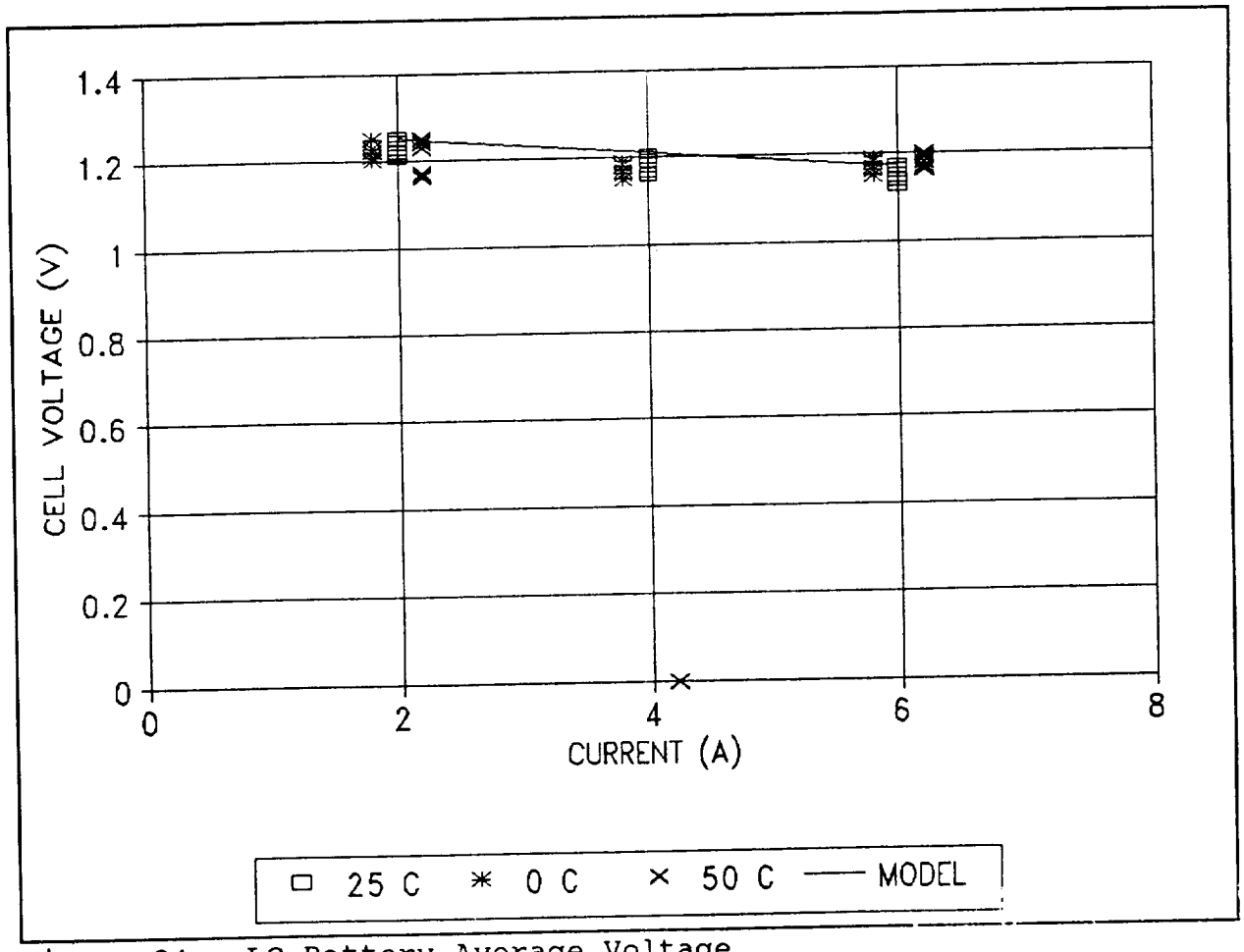

Figure 24: LC Battery Average Voltage

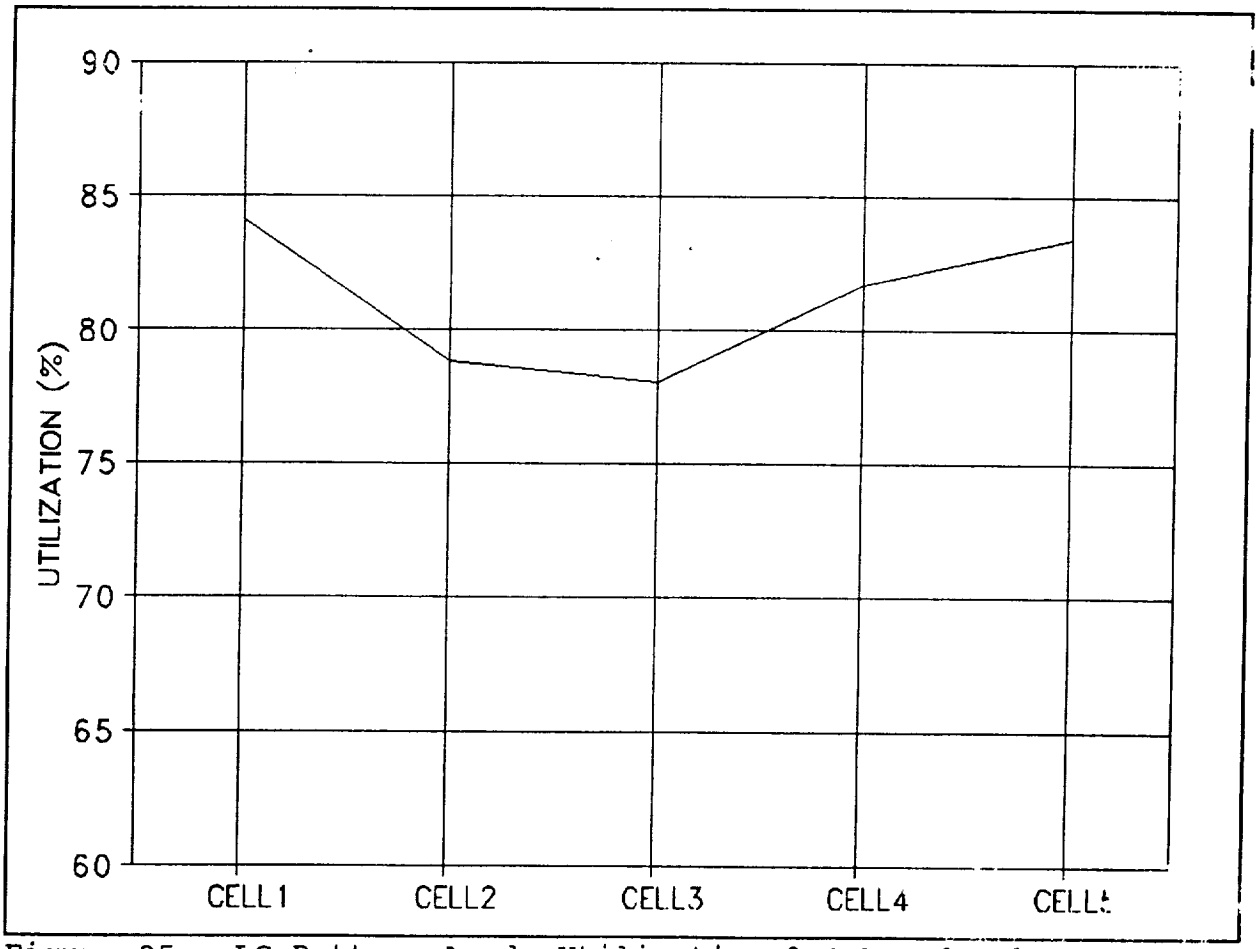

Figure 25: LC Battery Anode Utilization @ 6 A and 25° C

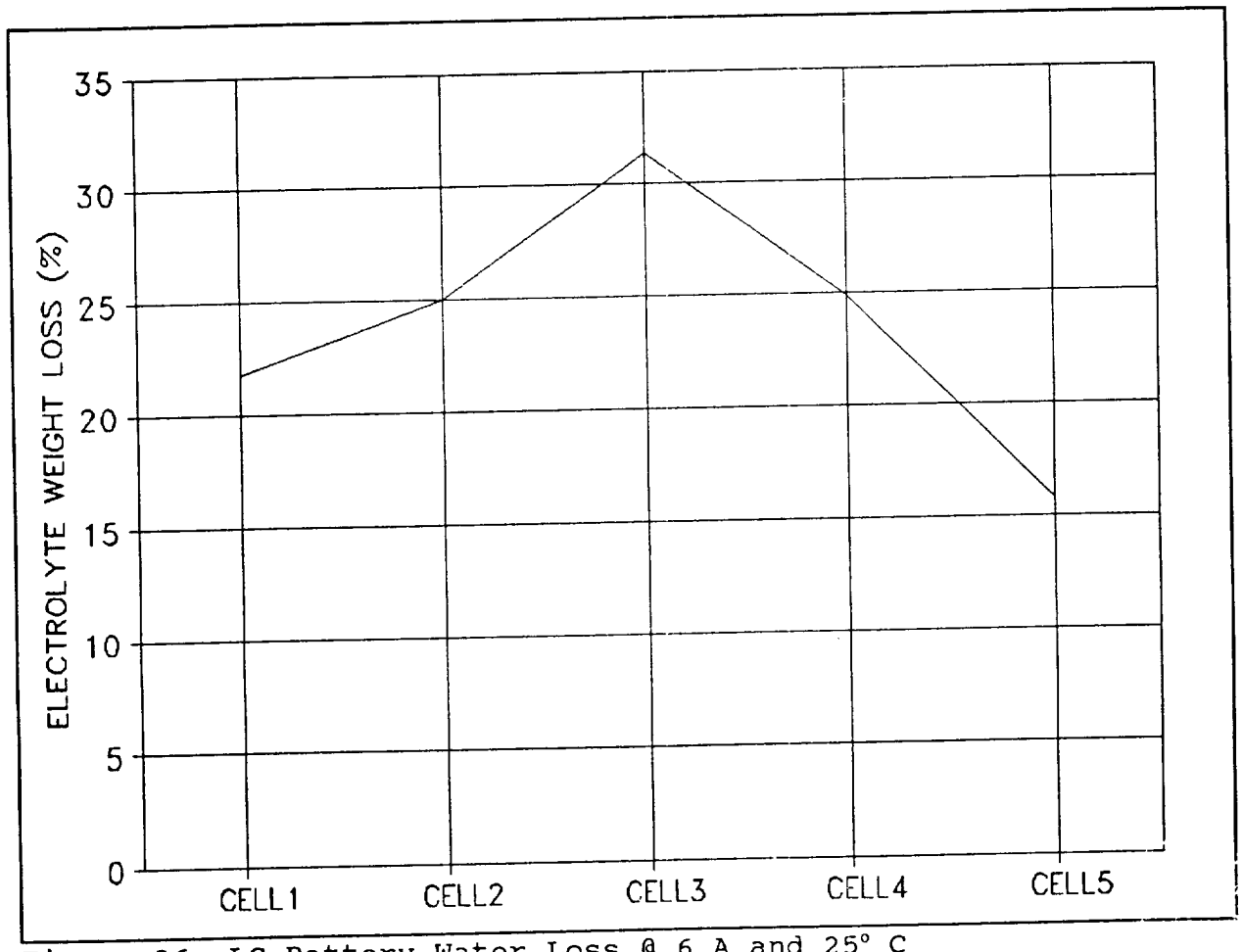

Figure 26: LC Battery Water Loss @ 6 A and 25° C

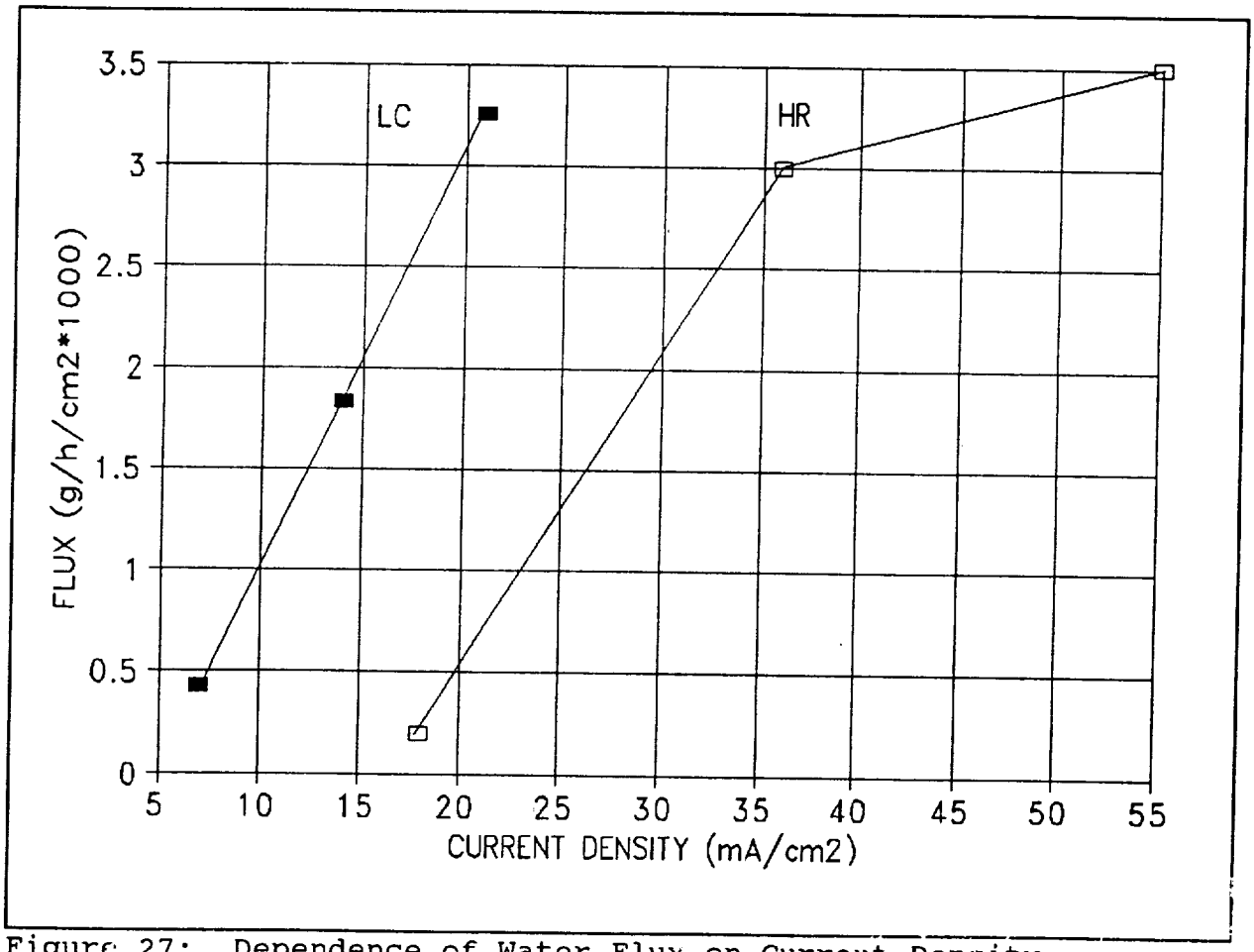

Figure 27: Dependence of Water Flux on Current Density